Title

Early TP53 alterations engage environmental exposures to promote gastric premalignancy in an integrative mouse model

Journal

Nature Genetics, 52(2)

ISSN

1061-4036

Authors

Sethi, Nilay S
Kikuchi, Osamu
Duronio, Gina N
et al.

Publication Date

2020-02-01

DOI

10.1038/s41588-019-0574-9

Peer reviewed

HHS Public Access

Author manuscript

Nat Genet. Author manuscript; available in PMC 2020 August 05.

Published in final edited form as:

Nat Genet. 2020 February ; 52(2): 219–230. doi:10.1038/s41588-019-0574-9.

Early TP53 Alterations Engage Environmental Exposures to Promote Gastric Premalignancy in an Integrative Mouse Model

Nilay S. Sethi[1,2,3,*], **Osamu Kikuchi**[1,10], **Gina Duronio**[1,10], **Matthew D. Stachler**[1,4,7,11], **James M. McFarland**[3,11], **Ruben Ferrer-Luna**[1,3], **Yanxi Zhang**[1], **Chunyang Bao**[1], **Roderick Bronson**[5], **Deepa Patil**[4], **Francisco Sanchez-Vega**[6], **Jie-Bin Liu**[1], **Ewa Sicinska**[7], **Jean-Bernard Lazaro**[8,9], **Keith L. Ligon**[1,3,7], **Rameen Beroukhim**[1,3], **Adam J. Bass**[1,2,3,*]

[1]Department of Medical Oncology, Dana-Farber Cancer Institute, Boston, MA 02215

[2]Gastrointestinal Cancer Treatment Center, Dana-Farber Cancer Institute, Boston, MA 0221

[3]Broad Institute of Massachusetts Institute of Technology and Harvard University, Cambridge, Massachusetts 02142

[4]Department of Pathology, Brigham and Women's Hospital, Boston, MA 02215

[5]Department of Pathology, Harvard Medical School, Boston, MA 02215

[6]Department of Surgery and Department of Epidemiology and Biostatistics, Memorial Sloan Kettering Cancer Center, New York, NY 10065

[7]Department of Oncologic Pathology, Dana-Farber Cancer Institute, Boston, MA 02215

[8]Center for DNA Damage and Repair, Dana-Farber Cancer Institute, Boston, MA 02215

[9]Department of Radiation Oncology, Dana-Farber Cancer Institute, Boston, MA 02215

[10]These authors contributed equally

[11]These authors contributed equally

Abstract

* nilay_sethi@dfci.harvard.edu (N.S.S.), adam_bass@dfci.harvard.edu (A.J.B.).

AUTHOR'S CONTRIBUTION:
Conception and design: N.S.S., A.J.B.
Development of methodology: N.S.S., A.J.B.
Mouse Studies: N.S.S., O.K., Y.Z.
Histopathology: M.D.S., R.Br., D.P., E.S.
Transcriptomics and genomics: N.S.S., J.M.M., C.B., F.S-V.
Pharmacogenomics: R.F-L., K.L.L., R.Be.
Other Investigations: N.S.S., O.K., G.D.
Resources: J-B.L.
Formal Analysis: N.S.S., O.K., G.D., A.J.B.
Writing – Original Draft: N.S.S., A.J.B.
Writing – Review and Editing: N.S.S., O.K., G.D., M.D.S., J.M.M., A.J.B.
Supervision: N.S.S., A.J.B.
Funding Acquisition: N.S.S., A.J.B.

COMPETING INTERESTS STATEMENT

N.S.S. is a consultant for HVH precision analytics. A.J.B has funding from Merck, Bayer and Novartis, is an advisor to Earli and Helix Nano and a co-founder of Signet Therapeutics.

Somatic alterations in cancer genes are being detected in normal and premalignant tissue, placing greater emphasis on gene-environment interactions that enable disease phenotypes. By combining early genetic alterations with disease-relevant exposures, we developed an integrative mouse model to study gastric premalignancy. Deletion of *Trp53* in gastric cells confers a selective advantage and promotes the development of dysplasia in the setting of dietary carcinogens. Organoid derivation from dysplastic lesions facilitated genomic, transcriptional, and functional evaluation of gastric premalignancy. Cell cycle regulators, most notably *Cdkn2a*, were upregulated by p53 inactivation in gastric premalignancy, serving as a barrier to disease progression. Co-deletion of *Cdkn2a* and *Trp53* in dysplastic gastric organoids promoted cancer phenotypes but also induced replication stress, exposing a susceptibility to DNA damage response pathway inhibitors. These findings demonstrate the utility of mouse models that integrate genomic alterations with relevant exposures and highlight the importance of gene-environment interactions in shaping the premalignant state.

INTRODUCTION

Gastric and esophageal (GE) adenocarcinomas carry dismal prognoses, often contributed to by their late-stage presentation[1]. A better understanding of the premalignant state that precedes neoplasia is therefore required. The development of faithful models of premalignancy can address this unmet need by informing prevention and early intervention strategies. Furthermore, these models can help define key elements of gene-environment interactions that govern the premalignancy to cancer transition[2].

GE adenocarcinomas bear striking similarities based on epigenetic[3], genomic/molecular[4], and cellular[5] features, suggesting that these cancers are related. Dysplasia is the premalignant state characterized by epithelial tissue with abnormal cellular architecture, nuclear atypia, and loss of cell polarity[6]. Dietary carcinogens and inflammation are critical insults in the evolution of premalignant gastric lesions. The unconjugated bile acid deoxycholate (DCA) is a principal component of gastroduodenal contents that promotes chronic inflammation in the stomach[7-9]. Nitrosamines are indirect dietary byproducts implicated in the pathogenesis of gastric premalignancy[10] and carry carcinogenic properties that increase the risk of cancer[11,12]. Indeed, rodent models have incorporated environmental exposures into the study of gastric adenocarcinoma[10,13-15]. Mouse models that incorporate the SS1 strain of *Helicobacter pylori* (*H. pylori*) and *H. felis* can recapitulate chronic inflammation, resultant gastritis and metaplasia, and eventually dysplasia[13,16-18]. By contrast, carcinogen exposure gives rise to a distinct model of gastric cancer by promoting dysplastic lesions and adenocarcinoma with relatively little to no metaplasia. Complementing these approaches, genetically-engineered mouse models (GEMMs) of stomach cancer have relied upon penetrant combinations of genomic alterations that drive malignant transformation with short latency[19-22].

TP53 is the most common recurrent mutation in gastric and esophageal adenocarcinoma[23-25]. It is now clear that premalignant lesions also incur early enabling mutations as evident from clonal hematopoiesis[26,27] and intestinal metaplasia, the most recognized precursor lesion to GE adenocarcinoma[28,29]. By comparing mutation patterns

from matched patient-derived premalignant Barrett's esophagus (BE) and esophageal adenocarcinoma lesions, we found that *TP53* is mutated early in the progression of GE malignancy, often occurring before dysplasia[24]. Deep sequencing of noncancerous gastric epithelium from patients with gastritis showed that just under half harbored *TP53* mutations[30]. Furthermore, we found that *TP53* is preferentially mutated in the subset of nondysplastic BE patients who progress to cancer[31]. This sequence of genomic events is notably different than other gastrointestinal cancers, such as colorectal or pancreatic, in which *TP53* is mutated relatively late in cancer development[32,33]. Based upon these observations, we hypothesized that chronic inflammation and carcinogenic exposures enable selection of *TP53* altered cells to promote premalignant lesions (Extended Data Fig. 1a). To test this hypothesis, we designed a new, integrative mouse model that combines disease-relevant exposures with tissue-specific *TP53* alterations to study the development of gastric premalignancy.

RESULTS

Environmental exposure model of gastric malignancy

Prior to studying the impact of *Trp53* (mouse *TP53*) in premalignancy, we established a gastric adenocarcinoma model in wildtype (WT) C57BL/6J mice by exposing them to drinking water containing deoxycholic acid (DCA) and N-methyl-N-nitrosourea (MNU)[15] (Extended Data Fig. 1b). MNU was selected based on the following: (a) it is a nitrosamide related to dietary nitrosamines implicated in human disease[34], (b) when compared to six other nitroso-compounds, it preferentially led to gastric disease[35], and (c) it promoted premalignant GE lesions in transgenic mice with endogenous inflammation[5,36]. Mice from this experiment were sacrificed after 18 months to evaluate gastric phenotypes. While untreated (n = 5) and DCA-alone treated (n = 7) mice did not develop premalignant lesions, 39% of MNU (n = 8) or DCA/MNU (n = 10) treated mice developed adenocarcinomas along the stomach lesser curvature (Extended Data Fig. 1c, Fisher's exact p-value = 0.03). Whole exome sequencing (WES) analyses in these lesions showed mutation signatures enriched for CT substitutions consistent with exposure to MNU, which cause the formation of O^6-alkylguanines[37] (Extended Data Fig. 1d). Mutational (single-nucleotide variants/insertion-deletions) and copy number (amplifications) analyses showed an inverse relationship (Extended Data Fig. 1e), consistent with a recent report using MNU-induced tumors[37]. Overall, these results indicate that dietary exposures can directly promote the development of gastric adenocarcinomas in C57BL/6J mice.

Lgr5-p53^{KO} mice display greater dysplasia with DCA/MNU

Our central hypothesis is that mutant p53 gastric cells promote premalignant lesions when subjected to disease-relevant exposures (Extended Data Fig. 1a). To test this hypothesis, we conditionally manipulated *Trp53* in distinct cell populations of the stomach. Our first model built upon the observation that Lgr5 marks antral gastric stem cells [38]. Transgenic mice with conditionally deleted *Trp53* or activated missense mutant (*Trp53*^{R270H}) in Lgr5+ cells were exposed to drinking water containing DCA and MNU as described previously (Fig. 1a) and sacrificed at 12 months to study premalignant lesions (Supplementary Note#1).

Deletion of *Trp53* in Lgr5+ cells of untreated mice did not lead to detectable premalignant lesions, suggesting that p53 loss alone is not sufficient to promote dysplasia (Fig. 1a-b). When treated with DCA/MNU, however, Lgr5-p53^{KO} mice demonstrated a 3.5-fold increase in dysplastic lesions compared to Lgr5-p53^{WT} mice (Fig. 1b-c). Dysplastic lesions occurred along the stomach antrum lesser curvature, consistent with the highest density of Lgr5+ cells[38]. Recombination-specific PCR demonstrated that Lgr5-p53^{KO} premalignant lesions lacked p53 (Extended Data Fig. 2a). WES showed that dysplastic lesions from treated Lgr5-p53^{KO} mice harbored a greater burden of mutations compared to Lgr5-p53^{WT} mice, consistent with p53 function in preserving the integrity of the genome (Fig. 1d). We also asked whether DCA or MNU alone could promote premalignant lesions in Lgr5-p53^{KO} mice. Only MNU containing regimens developed premalignant lesions in Lgr5-p53^{KO} mice, demonstrating the importance of carcinogens in this model (Extended Data Fig. 2d). These results indicate that p53 deletion in gastric stem cells engages carcinogenic exposures to promote premalignant lesions.

Mist1-p53^{KO} mice display greater dysplasia with DCA/MNU

To test whether p53 deletion in a distinct gastric compartment can promote premalignancy, we utilized *Mist1*-CreERT2 mice. Mist1 marks chief cells, which have been shown to respond to inflammation[39] and undergo neoplastic transformation following genetic alterations[19]. We crossed *Mist1*-CreERT2; *Trp53*$^{F/F}$ mice with *R26*-mTmG reporter mice to mark p53^{KO} with eGFP. *Mist1*-CreERT2; *R26*-mtmG mice served as controls in which Mist1+ p53^{WT} epithelial cells were marked by eGFP (Fig. 1e). Untreated Mist1-p53^{KO} mice did not develop dysplastic lesions for up to two years of monitoring, consistent with our results in Lgr5-p53^{KO} mice. Mist1-p53^{KO} mice, however, developed over 2.5 times as many dysplastic lesions as Mist1-p53^{WT} mice when subjected to DCA/MNU (Fig. 1f). Indeed, invasive gastric adenocarcinomas arose only in DCA/MNU treated Mist1-p53^{KO} mice (n = 2) at this early time-point. Immunohistochemical analysis for GFP demonstrated greater expansion of Mist1-p53^{KO} cells in dysplastic and polypoid lesions (Fig. 1g). These results demonstrate that p53 deletion in a distinct subpopulation of stomach cells promotes premalignancy when subjected to carcinogenic exposures.

Growth advantage of p53^{KO} premalignant cells exposed to MNU

To investigate the direct impact of DCA and MNU on premalignant cells, we optimized an *in vitro* culture system using human nondysplastic BE CP-A cells WT for TP53. Treatment with graded concentrations of DCA led to nonspecific toxicity without impacting p53 expression or cell cycle activity (Extended Data Fig 3a-c). MNU treatment, however, led to dose-dependent proliferation defects and G2/M growth arrest (Fig. 2a, Extended Data Fig. 3d). MNU also led to p53 induction (Fig. 2b) with dsDNA damage as shown by γH2Ax immunofluorescence (Fig. 2a), consistent with the carcinogenic effects of dietary nitrosamines. Together, these studies suggest that dietary nitrates can lead to growth arrest secondary to p53 induction and dsDNA damage.

We next asked whether MNU-induced phenotypes were dependent on p53 function *in vitro*. We engineered p53 knockdown (KD) and knockout (KO) CP-A cells using short-hairpin RNA (shRNA) and CRISPR/Cas9, respectively (Extended Data Fig. 3e). Inhibiting p53 did

not affect proliferation of untreated CP-A cells (Extended Data Fig. 3f). By contrast, CP-A $p53^{KO}$ cells exposed to MNU avoided G2/M arrest and gained a proliferative advantage relative to CP-A $p53^{WT}$ cells (Fig. 2c-e). CP-A $p53^{KO}$ cells displayed greater γH2Ax positivity with MNU treatment (Extended Data Fig. 3g), demonstrating the ability to tolerate greater DNA damage. To determine which genes/pathways enable these phenotypes, we performed mRNA sequencing (RNA-seq) of CP-A $p53^{KD}$ cells. In addition to the p53 pathway (Extended Data Fig. 2h-i), gene-set enrichment analysis (GSEA) showed downregulation of the DNA repair response in CP-A $p53^{KD}$ cells (Fig. 2f). These findings may explain the selective advantage of p53 altered premalignant cells in the setting of dietary carcinogens (Fig. 2g).

To evaluate the impact of MNU using another model system, we isolated gastric organoids from *Trp53*$^{F/F}$ mice and generated isogenic $p53^{KO}$ derivatives. $p53^{KO}$ gastric organoids displayed a growth advantage in MNU-containing media (Fig. 3a). We next performed competition assays using gastric organoids derived from dual-labelled R26-mtmG mice. eGFP+ Mist1-$p53^{WT}$ and Mist1-$p53^{KO}$ gastric organoids were isolated from their respective untreated, tamoxifen-induced mice. eGFP+ Mist1-$p53^{WT}$ gastric cells represented 1.3% of early passage cultures, which remained a stable relative proportion when passaged in DMSO control and MNU-containing media (Fig. 3b). By contrast, eGFP+ Mist1-$p53^{KO}$ gastric organoids, which initially represented 0.3% of early passage cultures, expanded by approximately 13-fold to 6.7% when passaged in MNU-containing media (Fig. 3b-c). We also evaluated $p53^{R270H/+}$ gastric organoids, where eGFP+ Mist1-$p53^{R270H/+}$ represented 14.8% of an early passage culture whereas td+ Mist1-$p53^{+/-}$ occupied 80.2% (Extended Data Fig. 4a-b). The proportion of GFP+, Mist1-$p53^{R270H/+}$ expanded by over 3-fold to 53.1%, whereas td+, Mist1-$p53^{+/-}$ decreased by 2-fold to ~40% when exposed to MNU (Extended Data Fig. 3b-c). These findings demonstrate a competitive advantage of p53-altered gastric organoids when exposed to dietary carcinogens (Extended Data Fig. 4d).

Genome doubling in dysplastic Lgr5-$p53^{KO}$ gastric organoids

We next derived organoids from dysplastic lesions to characterize and functionally study premalignant gastric epithelium. Gastric organoids were generated from the antrum of untreated and DCA/MNU-treated Lgr5-$p53^{WT}$ and Lgr5-$p53^{KO}$ mice at the 12-month end-point (Fig. 4a). *Trp53* deletion was validated in organoids derived from Lgr5-$p53^{KO}$ mice using recombination-specific PCR (Extended Data Fig. 5a) and Nutlin treatment, which induces apoptosis in $p53^{WT}$ cells (Extended Data Fig. 5b).

To investigate phenotypic properties, we cultured these organoids under ultra-low attachment conditions. dys-Lgr5-$p53^{KO}$ organoids formed 5-fold larger colonies compared to dys-Lgr5-$p53^{WT}$ (Fig. 4b). Since colony-forming ability may be a surrogate marker for renewal capacity[32], we examined whether dys-Lgr5-$p53^{KO}$ organoids contained a greater percentage of $eGFP^{+}$ Lgr5-expressing stem cells (Supplementary Note#2), finding a modest increase in Lgr5+ stem cells in dys-Lgr5-$p53^{KO}$ organoids (Fig. 4c, Extended Data Fig. 5c). To corroborate these findings *in vivo*, we performed GFP IHC to measure location and quantity of Lgr5+ cells in dysplastic lesions from DCA/MNU-treated mice. Only dysplastic lesions from Lgr5-$p53^{KO}$ mice demonstrated ectopic expression of Lgr5+ stem cells,

extending beyond the mucous gland base (Fig. 4d). These findings suggest that early p53 loss may confer renewal properties in gastric premalignancy.

Genome doubling is considered an intermediate state that often precedes aneuploidy[33,40,41] and chromosomal instability (CIN)[42,43]. Alterations in p53 are strongly associated with genome doubling and the CIN subtype in human gastric cancer. To test whether chromosome-level alterations were associated with p53 loss in gastric premalignancy, we evaluated chromosome counts of dys-Lgr5-p53^{KO} to dys-Lgr5-p53^{WT} organoids. Karyotype analysis of dys-Lgr5-p53^{KO} organoids demonstrated greater genome doubling (Fig. 4e). To test whether deletion of p53 in dysplastic Lgr5-p53^{WT} gastric organoids lead to genome doubling, we treated dys-Lgr5-p53^{WT} organoids with AdenoCre. *Ex vivo* p53 deletion did not lead to a significant increase in genome doubling, suggesting that genomic evolution toward a tetraploid state developed over time *in vivo* (Extended Data Fig. 5d). In agreement with previous literature[44,45], whole genome doubling is often observed in premalignant lesions with *TP53* mutations (Extended Data Fig. 5e). These results suggest that p53-null dysplastic gastric lesions from our mouse model capture the tetraploid state, an intermediate in cancer formation.

To determine whether dysplastic organoids were capable of xenograft growth, we injected them into the flanks of nude mice. Only organoids derived from dys-Lgr5-p53^{KO} mice were capable of outgrowth, with an inverse relationship between degree of genome doubling and latency to exponential xenograft growth (Fig. 4f). Histopathology showed cellular atypia with prominent nucleoli and disorganized glands with stratified multilayer epithelium (Extended Data Fig. 5f) and abundant Lgr5+ cells by immunofluorescence (Extended Data Fig. 5g). To evaluate somatic copy number (SCN) alterations, we performed low-pass whole-genome sequencing (LP-WGS) on dys-Lgr5-p53^{KO} cultured organoids and their derivative xenografts. Although SCN alterations were not detected in cultured organoids, their derivative xenografts demonstrated *broad* SCN gains and losses (Extended Data Figure 5h), unlike the focal events observed in human gastric cancer[43](Supplementary Note#3). The experiment did not distinguish between (1) the emergence of a clone that already existed in culture below the detection threshold for SCN assessment by LP-WGS or (2) the development of the chromosome instability in a dominant clone during xenograft growth. These data suggest that the premalignant gastric organoid system may enable the study of structural genomic alteration evolution.

Transcriptional profile of dysplastic Lgr5-p53^{KO} organoids

We next investigated the molecular mechanisms underlying the phenotypes observed in dysplastic Lgr5-p53^{KO} gastric premalignancy. Given the higher mutational burden in Lgr5-p53^{KO} dysplastic lesions (Fig. 2f), we first queried whole exome sequencing data for the presence of genes significantly mutated in human cancer. These analyses did not yield a clear pattern of mutations in Lgr5-p53^{KO} dysplastic gastric lesions (Supplementary Table 1). We therefore examined transcriptional profiles of dys-Lgr5-p53^{KO} compared to dys-Lgr5-p53^{WT} organoids (Fig. 5a). As expected, *Trp53* expression was attenuated in dys-Lgr5-p53^{KO} organoids (Extended Data Fig. 6a). GSEA identified pathways enriched in dys-Lgr5-p53^{KO} organoids (Fig. 5b), including inflammation, WNT/stem cell, and cell cycle

regulation. Among the inflammation pathways, interferon (IFN), TNFα, IL-6/Stat3, and IL-2/Stat5 signaling pathways were strongly upregulated (Fig. 5b). Four cytokines, *Csf3, Cxcl10, Crfl1 and Ccl5*, were consistently elevated in dLgr5-p53^{KO} organoids (Extended Data Fig. 6b)

To determine whether upregulation in these pathways is a direct consequence of p53 loss, we performed RNA-seq on isogenic p53^{KO} organoids (Fig. 3a). We reasoned that this comparison would reflect gene-expression changes in response to immediate p53 inactivation (Fig. 5a). Unexpectedly, most of the pathways found upregulated in dys-Lgr5-p53^{KO} organoids were downregulated in p53^{KO} organoids. In addition to the p53 pathway, epithelial-to-mesenchymal transition (EMT), inflammation-associated, hypoxia, and stem cell pathways were downregulated in p53^{KO} organoids compared to p53^{WT} (Extended Data Fig. 6c). This experiment suggested that either the duration of p53 loss or context of dysplasia contributed to the upregulation of these pathways in dys-Lgr5-p53^{KO} premalignant lesions (Extended Data Fig. 6e).

To distinguish between these scenarios, we examined gene expression profiles of organoids derived from nondysplastic gastric antrum tissue of untreated Lgr5-p53^{KO} and Lgr5-p53^{WT} mice. This comparison reflects gene expression changes in response to p53 inactivation that have occurred over a year *in vivo* without DCA/MNU (Fig. 5a). We plotted pathways enriched in dys-Lgr5-p53^{KO} (relative to dys-Lgr5-p53^{WT}) against nondysplastic Lgr5-p53^{KO} (relative to nondysplastic Lgr5-p53^{WT}) organoids to identify gene-sets selectively enriched with p53 loss in dysplasia (Fig. 5c). As anticipated, gene-sets associated with p53 signaling were downregulated in both dysplastic and nondysplastic Lgr5-p53^{KO} groups (Fig. 5c, blue). Pathways associated with mitotic spindle, cell cycle checkpoints, and DNA replication stress were preferentially upregulated in dys-Lgr5-p53^{KO} organoids (Fig. 5c, orange), which may be expected in dysplasia. Although elevated in nondysplastic Lgr5-p53^{KO} organoids, IFN signaling pathways were more potently upregulated in dys-Lgr5-p53^{KO} (Fig. 5c; red). Consistently, p53 mutant human gastric cancers demonstrated a significant correlation between *CCL5* mRNA expression levels and IFN signaling by single-sample GSEA (Extended Data Fig. 6d-e).

dys-Lgr5-p53^{KO} organoids also demonstrated greater enrichment in stem cell pathways, especially WNT (Fig. 5c, green). By contrast, the WNT pathway was downregulated in p53^{KO} organoids (Extended Data Fig. 6b). These findings agree with recent literature[46] and earlier results that implicated increased stem cell properties in p53^{KO} dysplasia (Fig. 4b-d; Extended Data 5c,g). To extend these results, we directly examined WNT pathway status in dysplastic gastric organoids. dys-Lgr5-p53^{KO} gastric cells demonstrated a modest 2-fold increase in WNT reporter activity (Extended Data Fig. 7a). Moreover, dys-Lgr5-p53^{KO} gastric organoids demonstrated elevated protein expression of WNT-target and stem cell transcription factor Sox9 by immunoblot (Figure 5d), which was not observed with p53 inactivation *ex vivo* or in nondysplastic organoids (Figure 5d), suggesting that the context of dysplasia is required. Consistently, only dysplastic lesions from Lgr5-p53^{KO} mice demonstrated overexpression of Sox9, whereas nondysplastic and dysplastic Lgr5-p53^{WT} lesions demonstrated normal Sox9 nuclear expression restricted to mucous gland bases (Figure 5e). To test whether WNT activation serves a functional advantage, organoids were

grown in WNT-independent media. Only dys-Lgr5-p53^{KO} organoids were able to grow in media without WNT, R-spondin, and Noggin (Extended Data Fig. 7c), suggesting that elevated endogenous WNT activity can confer niche-independent growth (Supplementary Note#4). Taken together, these data indicate that dysplastic p53-null gastric lesions may develop increased renewal properties and elevated WNT signaling, possibly explaining the lower frequency of WNT pathway alterations in human gastric cancer compared to colorectal cancer[43].

CDKN2A induction in dysplastic Lgr5-p53^{KO} gastric lesions

The third gene-set consistently enriched in dys-Lgr5-p53^{KO} organoids was cell cycle regulation (Fig. 5b-c), with *Cdkn2a* among the most significantly upregulated genes (Fig. 6a). mRNA levels of *Cdkn2a* were elevated two- to three-fold in p53^{KO} and nondysplastic Lgr5-p53^{KO} gastric organoids compared to their respective controls. However, dys-Lgr5-p53^{KO} gastric organoids displayed a greater than 10-fold increase in *Cdkn2a* mRNA levels relative to dys-Lgr5-p53^{WT} (Fig. 6b). *CDKN2A* expression and p53 activity is also inversely correlated in human gastric cancer (Extended Data Fig. 8a). We next asked whether p53 deletion in p53^{WT} gastric premalignancy induces *CDKN2A* expression. Although *CDKN2A* is absent in CP-A cells, we observed upregulation of other *CDKN1* and *CDKN2* gene family members in CP-A p53^{KD} cells (Extended Data Fig. 6b). Deletion of p53 in dys-Lgr5-p53^{WT} organoids led to elevated protein expression of p16^{INK4A}, a protein product of *CDKN2A* (Fig. 6c). To investigate whether p53 negatively regulates p16 expression *in vivo*, we examined nuclear p16^{INK4a} staining in Lgr5-p53^{KO} and Lgr5-p53^{WT} dysplastic lesions. Greater nuclear p16^{INK4A} staining (red) was observed in Lgr5-p53^{KO} dysplasia (focal areas marked by dotted lines) relative to Lgr5-p53^{WT} controls (Fig. 6d). Using tissue from the Mist-p53^{KO} mouse model, we observed greater nuclear p16 staining co-localized with eGFP + Mist-p53^{KO} cells in dysplastic lesions (Fig. 6e). These data indicate that inactivation of p53 leads to p16^{INK4A} induction in gastric premalignancy.

CDKN2A and *TP53* co-alteration promotes gastric premalignancy

We next examined the relationship between *CDKN2A* and *TP53* in human cancer genomic data [42]. *TP53*^{Altered}, *CDKN2A*^{WT} GE cancers, especially the CIN subtype, showed increased mRNA expression of *CDKN2A* (Fig. 6f, Extended Data Fig. 8c). There was also a subset of human gastric cancers with alterations in both *CDKN2A* and *TP53* (Fig. Extended Data 8c). Analysis of genomic alterations in human esophageal adenocarcinoma[23,47] also showed significant co-occurrence of *TP53* and *CDKN2A* alterations (Extended Data Fig. 8d). A combined data-set containing genomic alterations in patients with GE adenocarcinoma treated at our institution (Extended Data Fig. 6e, n = 1,299, q < 0.001) confirmed this pattern of *TP53* and *CDKN2A* co-alteration. In aggregate, these data support a model whereby *CDKN2A*/p16^{INK4A} is upregulated in p53-altered dysplasia and subsequently inactivated during cancer progression.

We hypothesize that *CDKN2A*/p16^{INK4A}, a cell cycle negative regulator, may attenuate progression of p53-altered gastric premalignancy. A correlate to this hypothesis is that abrogating *CDKN2A*/p16^{INK4A} may enable progression of p53-altered gastric premalignancy. To investigate this, *Cdkn2a* and *Trp53* were co-deleted in dys-Lgr5-p53^{WT}

organoids to generate double knockouts (DKO). In parallel, *Cdkn2a* alone was inactivated in dys-Lgr5-p53^{KO} gastric organoids (Fig. 7a). dys-Lgr5-p53^{WT}-DKO gastric organoids demonstrated increased colony-forming ability in ultra-low attachment culture (Fig. 7b). Deletion of *Cdkn2a* improved colony-forming ability of dys-Lgr5-p53^{KO} gastric organoids grown in media with or without WNT (Fig. 7c). Furthermore, only dys-Lgr5-p53^{WT}-DKO gastric organoids were capable of xenograft growth in the flanks of nude mice compared to dys-Lgr5-p53^{WT}-control, -sgP53^{KO}, and -sgP16^{KO} gastric organoids, although the latency before exponential growth was longer compared to dys-Lgr5-p53^{KO} organoids (~5.5 months vs. <3 months; Figure 7d vs Figure 4f). These data provide functional evidence that, following *TP53* loss in dysplastic gastric lesions, *CDKN2A* can serve as a checkpoint to block further progression.

Co-deletion of *CDKN2A* and *TP53* sensitizes to DDR blockade

We suspected that abrogation of *Cdkn2a* and *Trp53* may impart strain on cellular replication. CHK1 and CHK2 are downstream components of the ATR and ATM DNA-damage response (DDR) pathways, respectively, and are activated during replication stress. Indeed, phospho-CHK1 and phospho-RPA32, another indicator of replication stress, were induced in dys-Lgr5-p53^{WT}-DKO but not dys-Lgr5-p53^{WT}-control, -sgP53^{KO}, and -sgP16^{KO} gastric organoids (Fig. 7e). Furthermore, phospho-CHK1 is elevated when p53 is deleted in CP-A cells, which are *CDKN2A* deficient (Fig. 7g). These results indicated that premalignant lesions with co-alterations in *Cdkn2a* and *Trp53* activate checkpoint responses associated with replication stress.

These findings also implicated a potential for therapeutic sensitivity. Specifically, we hypothesized that if the CHK1 DDR pathway is activated in *Cdkn2a* and Trp53-co-altered dysplastic lesions, then eliminating this checkpoint may promote mitotic catastrophe and cell death. To test this hypothesis, we queried data from an unbiased pharmacogenomic screen of multiple cancer types (Ferrer-Luna, Ramkissoon, Ramkissoon, Homberg, Verreault et al., unpublished). Gastric cancer cell lines with co-disruption of *CDKN2A*/*TP53* showed significantly greater sensitivity to the CHK1/2 inhibitor AZD7762 compared to those with only one or neither gene altered (Fig. 7f, Extended Data Fig. 9a). Consistent with the drug-response, genetic knockdown of *CHK1* or *WEE1*, a downstream mediator of ATR-CHK1 DDR, but not CHK2 showed preferential dependency in *CDKN2A*/*TP53* co-disrupted gastric cancer (Extended Data Fig. 9b). To validate this dependency, we tested the sensitivity of two additional gastric cancer cell lines to a more potent CHK1/2 inhibitor, Prexasertib. KE39 is *TP53* mutant and *CDKN2A* wildtype, whereas GSU is *TP53* and *CDKN2A* co-disrupted. Consistently, GSU gastric cancer cells were significantly more sensitive to Prexasertib than KE39 cells (Extended Data Fig. 9c). Furthermore, GSU was also significantly more sensitive to AZD1775, a potent WEE1 inhibitor, compared to KE39 (Extended Data Fig. 9d). Together, these data suggest that co-disruption of *CDKN2A* and *TP53* may serve as a predictive biomarker for sensitivity to CHK1-WEE1 DDR inhibitors.

We next investigated whether co-inactivating *CDKN2A*/*TP53* in premalignant CP-A cells confers increased sensitivity to CHK1 inhibition. Deletion of p53 in p16^{INK4A}-deficient CP-A cells led to a significant increase in Prexasertib sensitivity at doses corresponding to

phopho-CHK1 inhibition (Fig. 7g). We also examined DDR pathway inhibition using our murine dysplastic organoids. dys-Lgr5-p53^{WT}-DKO gastric organoids demonstrated greater sensitivity to Prexasertib than dys-Lgr5-p53^{WT}-control (Fig. 7h-j, Extended Data Fig. 9e). Moreover, dys-Lgr5-p53^{KO}-p16^{KO} demonstrated even greater sensitivity to Prexasertib than dys-Lgr5-p53^{KO}-control gastric organoids (Fig. 7h-j, Extended Data Fig. 9e). To investigate other DDR pathway members, we tested ATR inhibitor AZD6738 and WEE1 inhibitor AZD1775. Although dys-Lgr5-p53^{KO}-p16^{KO} were not preferentially sensitive to ATR inhibition, they did show increased sensitivity to WEE1 inhibition (Extended Data Fig. 9f-g). Overall, these data suggest that co-disruption of *CDKN2A* and *TP53* in gastric premalignancy not only promotes cancer progression but also confers sensitivity to inhibition of the CHK1-WEE1 axis of the DDR pathway.

DISCUSSION

GE adenocarcinomas are molecularly similar cancers that arise in the setting of chronic inflammation and carcinogen exposure[6]. *TP53* mutations are not only found in premalignant lesions[24,30,48] but also predict progression to cancer [31]. However, deleting *Trp53* in gastric cells alone did not lead to dysplastic lesions after 2 years of observation in mice, suggesting that additional factors, such as pathogenic mutations or exposures, are necessary (Supplementary Note#5). These results guided the development of an integrative mouse model that combines p53 alterations with carcinogenic exposures to study gene-environment interactions in gastric premalignancy.

Given the regenerative capacity of the gut epithelial lining, a question that remains is how do *TP53* mutant clones persist? One explanation is that *TP53* mutations occur in gastric stem cells. Another explanation is that *TP53* inactivation promotes renewal features, enabling fixation of a *TP53* mutation. We observed complete eGFP+ p53^{KO} regions persist after a year, often showing expansion in dysplastic lesions, which suggests that p53 loss facilitates fixation and expansion of these clones under carcinogen exposure. Deeper analysis revealed that p53 loss in dysplasia can promote renewal properties, WNT pathway activation, and independence from exogenous WNT ligands. These results are consistent with functional studies in human gastric cancer organoids showing that co-alterations in *TP53* and *CDH1* lead to R-spondin independence and elevated basal WNT signaling[46]. Importantly, these transcriptional outputs and phenotypes were not observed by p53 inactivation alone. In our model, the combination of dysplasia and p53 loss was required, consistent with data that dysregulation of a single pathway may not be sufficient to induce dedifferentiation[49] (Supplementary Note#6). Mechanisms underlying WNT activation in p53-altered gastric dysplasia and *CDH1*/*TP53* co-altered gastric cancer require further elucidation. Notwithstanding, these data may explain the substantially lower rates of somatic alterations in *APC* or *CTNNB1* in gastric cancer compared to colorectal cancer (CRC)[43]. Arguing against tissue-specific predisposition, colitis-associated CRC, which also manifests with early *TP53* mutations similar to GE cancer, have dramatically lower rates of WNT pathway alterations[50]. Taken together, these data suggest that early *TP53* mutations in gastric premalignancy may promote WNT signaling without requiring additional mutations in the pathway (Supplementary Note#7).

The *CDKN2A* locus encodes two gene products—p14^{ARF} and p16^{INK4A51}. p14^{ARF} stabilizes p53 by physically inhibiting its ubiquitination by MDM2[52-56]. p16^{INK4A} leads to growth arrest by inhibiting CDK4/6 activity, Rb phosphorylation, and E2F-mediated cell cycle progression[57-61]. Unlike p53-p14^{ARF}, little is known about the functional interactions between p53 and p16^{INK4A}, which are thought to function on two parallel axes of cell cycle regulation. Although *CDKN2A* is frequently deleted, mutated, or hypermethylated in BE[62,63], these lesions do not always progress to cancer[24]. In fact, *CDKN2A* inactivation has even been associated with a reduced risk of progression to esophageal adenocarcinoma[64]. By contrast, *TP53* mutations were found in matched premalignant/cancer lesions[24], and also predicated progression to cancer in patients with nondysplastic BE[31]. However, cell cycle regulators, such as p16^{ink4a}, likely serve as a critical break in GE lesions that have lost p53 function. Amplification of cyclins is another mechanism to circumvent cell cycle distress signals in p53-mutant GE adenocarcinomas, with *CCNE1* amplifications being mutually exclusive with *CDKN2A* inactivation[43], highlighting the importance of overcoming this checkpoint. Co-inactivation of *TP53* and cell cycle regulators can lead to reprogramming of cellular identity. Co-deletion of *TP53* and *RB* endowed neuroendocrine differentiation and resistance to enzalutamide in prostate cancer via SOX2 induction[65,66] (Supplementary Note#8). An open question that remains is whether *CDKN2A* and *TP53* co-inactivation in GE cancer promotes an alternative cellular state.

p16^{INK4A} induction in our model may represent a response to DNA damage[67] in the absence of p53. Inactivation of p16^{INK4A} appeared to increase replication stress (Figure 7d,g), rendering the DDR even more critical. DDR and replication stress are inappropriately activated in premalignant lesions and postulated to protect against progression to malignancy[68,69]. These DDR checkpoints and unscheduled replication may also generate new sensitivities in specific genomic contexts. p53-deficient cancer cells have exhibited a selective sensitivity to CHK1 inhibition when treated with cytotoxic agents or gamma-radiation[70]. Upstream of CHK1, ATR inhibition imparted selective toxicity in ATM- and p53-deficient cancer cells[71]. Inactivation of *CDKN2A* in head and neck cancer induced replication stress and conferred sensitivity to CHK1 inhibition[72]. Therefore, inactivation of p16^{INK4A} and p53, two critical regulators of cell cycle progression and DDR, may increase sensitivity of gastric cancer to CHK1 and WEE1 inhibitors. CIN- gastric cancers may particularly be susceptible to these inhibitors.

By combining early genomic alterations in *Trp53* with disease-relevant exposures, we generated an integrative mouse model that yielded new insights into critical gene-environment interactions that promote gastric premalignancy, identifying barriers to transformation and ultimately nominating a new therapeutic approach for this deadly cancer.

Methods

Animal Studies

All procedures involving mice and experimental protocols were approved by Institutional Animal Care and Use Committee (IACUC) of Dana-Farber Cancer Institute (11-009). The generation of *Lgr5*-EGFP-Ires-CreER^{T2} mouse was described earlier [74]. *Lgr5*-EGFP-Ires-CreER^{T2} mice were backcrossed in C57BL/6J mice and subsequently SNP tested to ensure

>97% pure background (Taconic). The generation of *Mist1*-CreER^{T2} mouse (kindly provided by Timothy Wang) was previously described [75]. To inactivate p53 in gastric tissue, we crossed Trp53$^{flox/flox}$ mice to *Lgr5*-EGFP-Ires-CreER^{T2} and *Mist1*-CreER^{T2} mice. To activate endogenous expression of p53^{R270H} in gastric tissue, we crossed *Trp53*$^{LSL\text{-}R270H}$ mice (kindly provided by Kwok Wong, NYU Langone Medical Center) to *Lgr5*-EGFP-Ires-CreER^{T2} or *Mist1*-CreER^{T2} mice. Compound *Mist1*-CreER^{T2}; *Trp53* mice were further crossed to *R26*-mtmG (kindly provided by Timothy Wang, Columbia University) mice for conditional eGFP labeling of Mist1+ gastric cells.

To activate conditional alleles, experimental mice aged 6–8 weeks were injected intraperitoneally with five consecutive daily 200 ml doses of tamoxifen in sunflower oil at 10 mg/ml to activate. For experiments with *Lgr5*-EGFP-Ires-CreER^{T2}, control mice did not receive tamoxifen; a subset of control mice were Cre-negative and did receive tamoxifen. For experiments with *Mist1*-CreER^{T2}; *R26*-mtmG mice, control mice without *Trp53* allele received tamoxifen. All treated mice were subjected to drinking water containing 240ppm of N-methyl-N-nitrosourea (MNU; biokemix) scheduled every other week for 6 weeks and/or 0.3 % deoxycholic acid (DCA; sigma) continuously for 1 year (or 1.5 year for p53^{WT} experiment in Extended Data Fig. 1. Mice were euthanized at the endpoint of the experiment, and stomachs were harvested for histopathological and immunohistochemical analyses as well as organoid generation.

A subset of mice unexpectedly developed thymic lymphomas when treated with MNU. These events were restricted to *Trp53*$^{LSL\text{-}R270H}$ mice, which harbors the conditional LSL-p53^{R270H} allele at the endogenous locus of p53 to facilitate expression under endogenous genomic conditions once activated by Cre/tamoxifen. An untoward effect however is that the endogenous wildtype p53 allele is knocked out. As a result, the mutant LSL-p53^{R270H} mice are heterozygous for p53 (+/−) in every tissue and can only conditionally express p53^{R270H} wherever Cre is activated. Nevertheless, in the setting of MNU exposure, the p53 +/− thymic tissue appears to be susceptible to losing the remaining wildtype copy and developing thymic lymphomas reliably within 3-4 months of carcinogen exposure initiation. Therefore, the development of thymic lymphomas in these mice is unrelated to Lgr5-Cre expression, which, to our knowledge, is not expressed in T-cells or other immune cells. As shown in Extended Data Fig. 2c, all MNU-treated mice, irrespective of tamoxifen induction, began to die around 100 days after the experiment was initiated. In other words, MNU-treated mice in which mutant p53^{R270H} was not activated (green) or Lgr5-Cre was not present (orange), still died due to thymic lymphoma complications.

For tumor xenografts, 1×10^6 organoid cells were injected into flanks of athymic Ncr-nu/nu mice. Tumor measurements were made by caliper and tumor volumes were calculated using the formula: volume = length × width^2 × 0.5. At the end-point of experiments, tumors were harvested, fixed in 10% formalin overnight, and paraffin-embedded for histological analysis. Fresh tissue was also collected for DNA isolation and flash-frozen for long-term storage.

Histopathology

Paraffin-embedded murine stomachs were serially sectioned and mounted on a slide. Hematoxylin and eosin (H&E) and Alcian blue stains were used to evaluate evidence of

dysplasia and metaplasia, respectively. The slides were reviewed by three pathologists, two with subspecialty training in gastrointestinal diseases (MDS and DP) and one specializing in rodent pathology (RB) for the presence of dysplasia. For molecular studies, areas of metaplasia and/or dysplasia were marked on the H&E slide and used as a guide for macrodissection on serial unstained slides.

Human samples: Previously published whole exome sequencing data of laser capture microdissected areas of Barrett's esophagus, Barrett's with low/high grade dysplasia, and esophageal adenocarcinoma from esophagectomy specimens was reviewed for TP53 mutations, whole genome doubling, and copy number changes[24]. Areas of high grade dysplasia were seen that had TP53 mutations and WGD, suggesting that both develop before invasion.

Immunofluorescence and immunohistochemistry

Primary stomach tissue and organoid xenograft tumors were excised and fixed with 10% formalin overnight and embedded in paraffin (FFPE). Unstained sections were stained using the following protocol. The immunofluorescence antigen labeling of the paraffin-embedded murine stomach samples was performed with P16INK4 antibody. The paraffin sections were deparaffinized and rehydrated, followed by antigen retrieval using sodium citrate buffer (pH 6). After three washes with TBS, the sections were incubated with 5% normal donkey serum (Jackson ImmunoResearch Lab Inc, West Grove PA) for an hour at room temperature. Slides were then incubated with mouse anti-P16INK4 (1:1000, Abcam, ab 54210) primary antibody overnight at 4°C. The slides were washed three times and incubated with Cy3 conjugated Donkey anti-mouse secondary antibody (Jackson ImmunoResearch Lab, 1:300), and Alexa Fluor 647 conjugated Donkey anti-mouse secondary antibody (Invitrogen, 1:300). Samples were counterstained with Hoechst and then washed three times with TBS, and the slides were mounted with Prolong Gold anti-fade mounting media (Invitrogen).

The double immunofluorescence antigen labeling of the paraffin-embedded murine stomach samples was performed with P16INK4 and GFP antibodies. The paraffin sections were deparaffinized and rehydrated, followed by antigen retrieval using sodium citrate buffer (pH 6). After three washes with TBS, the sections were incubated with 5% normal donkey serum (Jackson ImmunoResearch Lab Inc, West Grove PA) for an hour at room temperature. Slides were then incubated with mouse anti-P16INK4 (1:1000, Abcam, ab 54210) and goat anti-GFP (1:500, Novus Biologics, NB100-1678) primary antibodies overnight at 4°C. The slides were washed three times and incubated with Cy3 conjugated Donkey anti-mouse secondary antibody (Jackson ImmunoResearch Lab, 1:300), and Alexa Fluor 647 and Alexa Fluor 488 conjugated Donkey anti-goat secondary antibody (Invitrogen, 1:300). Samples were counterstained with Hoechst and then washed three times with TBS, and the slides were mounted with Prolong Gold anti-fade mounting media (Invitrogen).

Gastric Organoid Culture

Isolated gastric glands were counted and a total of 100 glands mixed with 50 ml of Matrigel (BD Bioscience) and plated in 24-well plates. After polymerization of Matrigel, conditioned media containing WNT, R-spondin, and Noggin was added and changed every 3-4 days. For

the first 2 days after seeding, the media was also supplemented with 10 mM ROCK inhibitor Y-27632 (Sigma Aldrich) to avoid anoikis. For passage, gastric organoids were removed from Matrigel, mechanically dissociated, and transferred to fresh Matrigel. Passage was performed every week with a 1:5–1:8 split ratio. For colony formation experiments, equal number of gastric organoids were plated without Matrigel in ultra-low attachment plates. Colony size was measured by ImageJ software from representative images.

Recombination specific quantitative PCR

Genomic DNA was extracted from gastric organoids using the AllPrep DNA/RNA Mini Kit (Qiagen) according to the manufacturer's instruction. Real-time PCR was performed and analyzed using CFX96 Real-Time PCR Detection System (Bio-Rad Laboratories, Inc.) and using Power SYBR Green PCR Master Mix (Thermo Fisher Scientific) according to the manufacturer's instructions. Relative DNA amount was determined by normalizing to Gapdh, which served as an internal control. Primers used are listed in Supplementary Table 3.

Karyotype Analysis

Gastric organoids were dissociated in TrypLE and then incubated in 10 ml of WRN media containing 100 ul of Colcemid (Irvine Scientific, 10 microgram/mL) for 3 hours at 37°C. Organoids were then rinsed with 5mL of warmed HBSS and then incubated in 3.5 mL of warmed HBSS containing 0.05% Trypsin (Gibco for 3-5 minutes at 37°C. Organoids were then spun down at 1200 RPMs for 10 min after adding 7.5 mL of HBSS media to the cell suspension. After media was aspiration, organoids were gently vortexed and then resuspended in 1 mL of 0.075M potassium chloride (KCl) by adding solution in a dropwise while stirring. An additional 9 mL of 0.075M KCl was added and incubated at room temperature for 20 min. 1mL of 3:1 methanol:acetic acid fixative was then added and mixed by inverting tube. Organoids were pelleted at 1200 rpms for 10 min and gently vortex after removing supernatant. Fixation with 3:1 methanol:acetic acid was repeated 3-5 times before long-term storage at −20°C or short-term storage in 4°C. A drop of cell pellet was added to a slide, stained with Giemsa, and counted.

Cell Culture, Lentivirus Project, and Transduction

CP-A are premalignant Barrett's metaplasia cells obtained from ATCC and cultured in keratinocyte media supplemented with calf bovine serum and EGF. KE39 and GSU are human gastric cancer cell lines obtained from the CCLE core facility, which obtained them directly from commercial sources and authenticated the lines using standard STR analysis.

Cell Proliferation Assays

Cell viability was quantified by measuring cellular ATP content using the CellTiterGlo Cell Viability assay (Promega) according to the manufacturer's instructions. All experiments were performed in triplicate in 96-well plates. Area measurements and quantification of low-attachment colonies was measured using ImageJ software.

Generation of knockout and knockdown cell lines

All genetically engineered gastric organoid lines were generated using the protocol described in Shalem, et al. [76]. In brief, sgRNAs targeting *TP53*, *Trp53*, and *Cdkn2a* were designed, amplified, and cloned into Lenti-CRISPR v2 [77]. shRNAs targeting *TP53* were cloned into PLKO.1 and TET-PLKO vectors. Lentivirus was generated using standard protocols. HEK-293T cells were plated in 10-cm^2 plates with fresh medium without antibiotics. Subsequently, 5 μg of the target plasmid, 1.25 ug of the envelope plasmid (pMD2.G) and 3.75 ug of the packaging plasmid (psPAX2) were diluted in Opti-MEM (Thermo Fisher Scientific, Cambridge, MA, USA; #31985070) and 30 μl of X-tremeGene 9 DNA transfection reagent (Millipore Sigma; #036335779001) was added dropwise and this mixture was incubated for 20 min. The DNA complexes were added dropwise to the cells and incubated for 12 h before aspirating and addition of 6 ml of fresh medium. Virus-containing supernatant was collected and passed through a 0.45-μm pore cellulose acetate filter at 24 and 48 h post-transfection; lentivirus was either immediately used to infect target cell-lines/organoids and/or stored at −80 °C.

RNA isolation and qPCR

Total RNA was isolated using the RNeasy Mini Kit (Qiagen, Germantown, MD, USA) and cDNA was synthesized using the Taqman Reverse Transcription Reagents kit (Thermo Fisher Scientific) according to the manufacturer's instructions. Gene-specific primers for SYBR Green real-time PCR were either obtained from previously published sequences or designed by PrimerBLAST (https://www.ncbi.nlm.nih.gov/tools/primer-blast/) and synthesized by Integrated DNA Technologies or ETON biosciences. Real-time PCR was performed and analyzed using CFX96 Real-Time PCR Detection System (Bio-Rad Laboratories, Inc., Hercules, CA) and using Power SYBR Green PCR Master Mix (Thermo Fisher Scientific) according to the manufacturer's instructions. Relative mRNA expression was determined by normalizing to *GAPDH* expression, which served as an internal control. See Supplementary Table 3 for primers used for qPCR.

Immunoblot, antibodies and inhibitors

Western blot analysis was performed as previously described [78]. Briefly, cells were lysed in RIPA buffer supplemented with a protease inhibitor cocktail. Whole cell extracts were resolved by SDS-PAGE, transferred to nitrocellulose membranes, and probed with indicated primary antibodies. Bound antibodies were detected with horseradish peroxidase (HRP)-conjugated secondary antibodies and chemiluminescent HRP substrate. Western blot analysis was performed as previously described [78]. Briefly, cells were lysed in RIPA buffer supplemented with a protease inhibitor cocktail. Whole cell extracts were resolved by SDS-PAGE, transferred to nitrocellulose membranes, and probed with indicated primary antibodies. Bound antibodies were detected with horseradish peroxidase (HRP)-conjugated secondary antibodies and chemiluminescent HRP substrate. The following primary antibodies were used for western blotting (all from Cell Signaling Technologies, Beverly, MA, USA, except where indicated): The following primary antibodies were used for western blotting (all from Cell Signaling Technologies, Beverly, MA, USA, except where indicated): anti-p53 (2524, 1:1,000), anti-CDKN2A (1:1000, 10883-I-AP, Protein Tech), anti-

pChk1(S345) (1:1000, 23415), anti-Chk1 (1:1000, 2360), anti-γH2AX (1:1000, 7631), anti-CDC2 (1:1000, 77055), anti-pCDC2(Y15) (1:1000, 9111), anti-pRPA32(S33) (1:1000, A300-236A, Bethyl Laboratories), Anti-ATR (1:1000, 2790), anti-pATR(S428) (1:1000, 2853), and anti-β-Actin (A5441, 1:1,000, Sigma). The following chemical drugs were used: AZD7762 and Prexasertib are CHK1/2 inhibitors, AZD1775 is a WEE1 inhibitor, and AZD6738 is an ATR inhibitor. All of which were employed at indicated concentrations and durations.

Whole exome sequencing analysis

We performed whole exome sequencing on the formalin-fixed paraffin embedded tissues. Exome sequencing, data processing, and mutation and somatic copy-number aberration analysis were performed, as previously described [31]. The reads were aligned to the reference sequence mm9 using BWA [79]. The alignments were further refined using the GATK for localized realignment around indel sites [80]. Recalibration of the quality scores was also performed using the GATK. The median coverage for the tumors is 89x. Mutation analysis for single nucleotide variants (SNV) was performed using MuTect v1.1.4 [81] and annotated by annovar[82]. The SomaticIndelDetector tool that is part of the GATK for indel calling was used. The mutational signatures were generated by SignatureAnalyzer [83]. Copy number variants were identified using Control-FREEC [84].

Low-pass whole genome sequencing (LP-WGS) analysis

LP-WGS was performed on DNA from tumor samples ($n = 6$). DNA for tumor samples was fragmented to approximately 390 bp. Indexed libraries were sequenced on an Illumina NextSeq (Illumina) to generate on average 20 million single-end 75 bp reads per sample. The mean LP-WGS coverage was 1-fold for the tumor samples. Reads were aligned to the mm10 genome. Copy number analysis was performed using QDNASeq[85]. The genome was divided into nonoverlapping 50-kb bins, and the number of reads mapping within each bin was counted and adjusted with a simultaneous 2D locally estimated scatterplot smoothing (LOESS) correction accounting for read mappability and GC content. All samples were also filtered for variants observed in a panel of three controls. All other QDNASeq parameters were set as default.

Differential expression analysis

We first excluded genes which had fewer than 1 count per million in at least 6 samples in each experiment. The weighted trimmed mean of M-values method [86] was used to normalize the library size of each sample, using the calcNormFactors function from the R package: edgeR [87]. Spearman correlation analysis of the log-transformed and library-size-normalized expression profiles for each sample, as well as visualization of the top two principal components, clearly identified one replicate sample as an outlier. This outlier sample was removed from all subsequent analysis.

To estimate log-fold change (LFC) differences, and associated p-values, between sample groups we used the R package limma [88]. Read counts data were transformed using the limma function ‘voom’ prior to model fitting, in order to model the mean-variance relationship of the log-counts data [89]. For analysis of the *in-vivo* data, multiple biological

replicates were sampled from each animal, and we modeled within-animal correlations across replicates using the 'duplicateCorrelation' function of limma. P-values were estimated from the empirical-Bayes moderated t-statistics, and q-values were estimated using the Banjamini-Hochberg method [90].

Gene set enrichment analysis (GSEA) [91] was run to test for gene sets that were up- or down-regulated in each experimental condition in a subset of experiments. In particular, we used the R package fgsea [92] to estimate normalized enrichment statistics, and associated p-values, for each gene set in the Hallmark Collection from the Molecular Signatures Database [93]. The GSEA algorithm was run using log-fold-change values as the gene-level statistics, 100,000 random permutations, and a "GSEA parameter" of 1. For this analysis, we also mapped mouse genes to human genes using the biomaRt "getLDS" function. For cases where multiple mouse genes were mapped to the same human gene, we averaged their t-statistics to produce one score per human gene prior to running GSEA analysis.

Cancer cell line analysis

Cancer cell line omics data were taken from the Cancer Cell Line Encyclopedia [refs]. Mutation calls and mRNA expression data were all taken from the Dependency Map 19Q1 data release, and can be accessed at depmap.org. CCLE cell line TP53 status was obtained from the DepMap 19Q1 mutation calls file. Cell lines with any non-silent mutation in TP53 were classified as TP53 mutant, and the remaining lines were classified as TP53 WT. Single-sample GSEA enrichment scores [94] were calculated for the Hallmark INTERFERON_GAMMA_RESPONSE and P53_PATHWAY gene sets [MSigDB ref], using the R package GSVA [95]

Pharmacological Screening

A total of 30 stomach cancer cell lines previously characterized at Cancer Cell Line Encyclopedia project [96] were queried for molecular dependencies and drug sensitivities. Somatic copy number alterations (SCNA), mutations and dependencies data for each cell line are available at Dependency Map (https://depmap.org) (18Q4 data release). Primary drug response or sensitivity data for stomach cancer cell lines are available at NCI-CTD2 Data Portal (ctd2.nci.nih.gov) (CTRP v2, 2015). In briefly, concentration-response curves for each cell line tested to AZD-7762 were fitted with nonlinear sigmoid functions. The area-under-curve (AUC) parameter was inferred by numerically integrating under the 16-point concentration-response curve [97]. The areas under percent-viability curves (AUC) were used as a robust measure of sensitivity and drug response, this metrics takes into account drug potency and efficacy.

To identify drug sensitivities associated with genetic alterations, we used PARIS [98] an algorithm that uses mutual information-based metric to rank dependencies (genetic features) based on the degree of correlation to the chemical profile (target profile, AZD-7762). The drug chemical profile input (target profile) was a continuous vector that included AUC value in each stomach cell line sample.

A total of 13 genetic features (Mutations and SCNA of the most frequently altered genes involved in cell cycle and DNA damage response) were queried against AZD-7762 in order

to predict response. For each interaction (genetic feature-drug), a metric based on the estimation of differential mutual information (RNMI) between the chemical profile of interest (target profile) and each genetic feature in the data was inferred. The differential mutual information was normalized based on the joint target-feature entropy, providing a universal metric (RNMI score) that took into account differences in entropy across essentiality profiles. In this way a perfect match or anti-match corresponded to an RNMI score of +1 or −1, respectively, while a random match corresponds to 0. The significance of a given RNMI matching score was estimated by an empirical permutation test and reported as a False Discovery Rate (FDR)[98]. Pharmacogenetic interactions were considered statistically significant when FDR ≤ 0.05.

Genetic Dependencies

To evaluate genetic dependencies, we interrogated the genetic dependency combined RNAi dataset at DepMap portal (https://depmap.org) (18Q4 data release), which is a public catalog of essential genes and dependencies for cell line proliferation as determined by genome-wide RNAi screening in three public available dataset (Achilles, Novartis and Marcotte). For 23 stomach cancer cell lines, a combined dependency score was available for queried genes (*CHEK1*, *CHEK2*, and *WEE*). Higher negative values of combined RNAi dependency score represent higher dependency for that gene.

Statistical analysis and reproducibility

Data are represented as mean ± s.d unless indicated otherwise. For each experiment, independent cell culture or technical replicates are noted in the figure legends. Statistical analysis was performed using Microsoft Office statistical tools or in Prism 7.0 (GraphPad). Pairwise comparisons between groups (that is, experimental versus control) were performed using an unpaired two-tailed Student's *t*-test or Kruskal–Wallis test as appropriate unless otherwise indicated. For all experiments, the variance between comparison groups was found to be equivalent. For xenograft experiments, data are displayed as mean ± s.e.m. and statistical comparisons were performed using unpaired, two-tailed Student's *t*-tests with Welch's correction. Animals were excluded from analysis if they were euthanized due to health reasons unrelated to tumor volume end-point. For *in vivo* experiments, all mice were randomized before studies.

Data Availability

All requests for raw and analyzed data and materials should be directed to corresponding authors. Data and materials that can be shared will be released via a material transfer agreement. Raw and processed RNA sequencing data have been deposited online with the accession number GSE141625. Raw genome sequencing data has been depoisted online with the accession number PRJNA594147 and PRJNA594086. Significantly mutated gene list from whole exome sequencing is available online in Supplementary Table 1. All Extended and Source Data are available online.

Extended Data

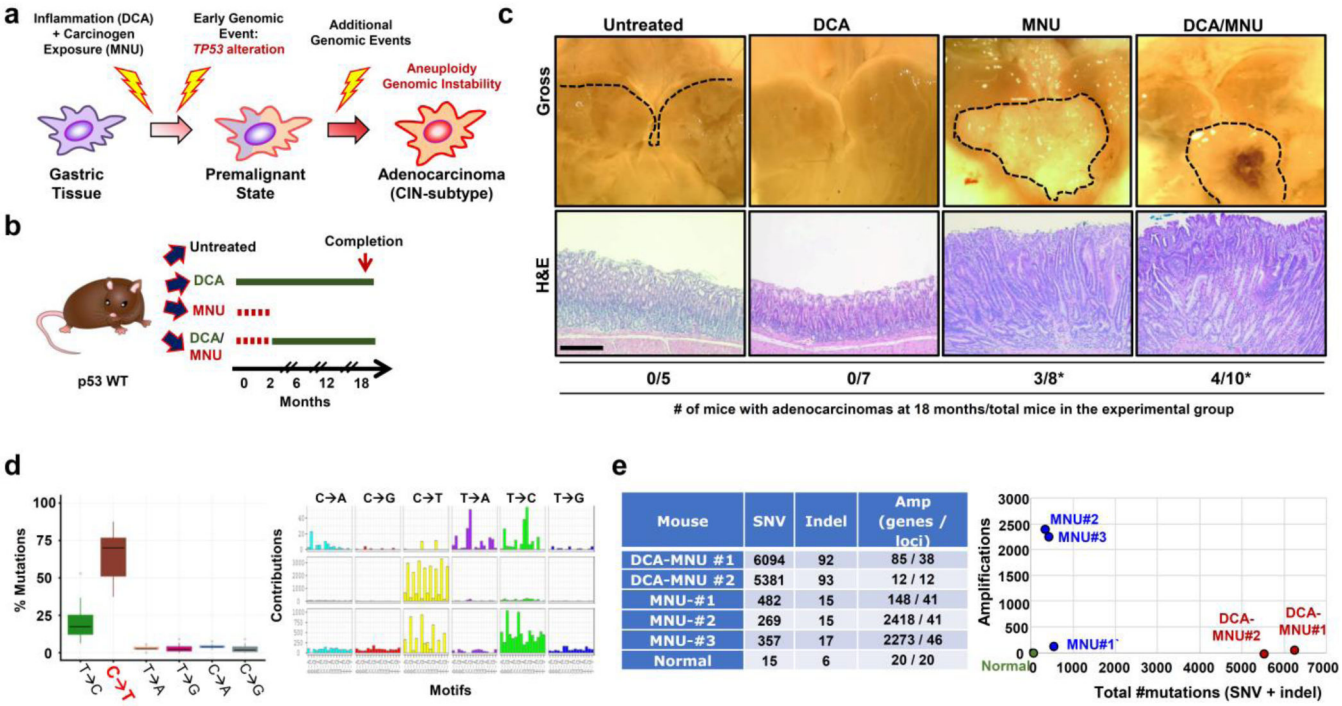

Mouse	SNV	Indel	Amp (genes / loci)
DCA-MNU #1	6094	92	85 / 38
DCA-MNU #2	5381	93	12 / 12
MNU-#1	482	15	148 / 41
MNU-#2	269	15	2418 / 41
MNU-#3	357	17	2273 / 46
Normal	15	6	20 / 20

Extended Data Fig. 1. Dietary carcinogen exposure promotes premalignant and malignant gastric lesions

(a) Schematic of central hypothesis: Chronic inflammation and carcinogen exposure collaborate with early genomic alterations (e.g. TP53 mutations) to enable the development of premalignant gastric lesions and eventual invasive cancer

(b) Schematic of p53 ^{WT} mice treated with DCA, MNU, or DCA+MNU combination for 18 months.

(c) Dissection microscope images of lower esophagus and stomach flayed open along greater curvature (top panel) and histopathological H&E staining (bottom panel) of gastric antrum. *A subset of mice died before the endpoint of the experiment due to other carcinogen-induced cancers (e.g. thymomas). Scale bar = 125μM

(d) Mutation signature analysis shows C→T changes characteristic of alkylating agent associated Signature 11. center line: median, lower hinge: the first quartile (Q1), upper hinge: the third quartile (Q3), extreme of the lower whisker: Q1 – 1.58 * (Q3 – Q1)/sqrt(n), extreme of the upper whisker: Q3 + 1.58 * (Q3 – Q1)/sqrt(n), n = 5.

(e) Mutation burden and copy number analysis of gastric lesions (n=5).

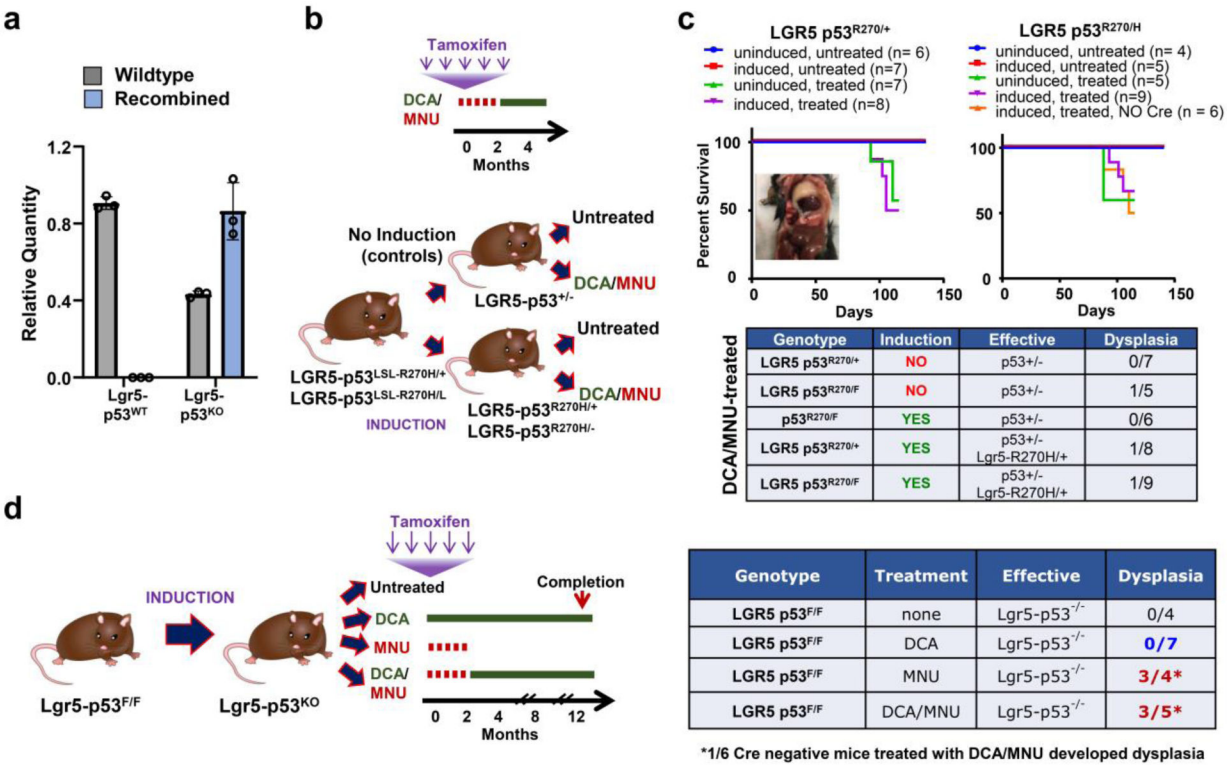

Genotype	Induction	Effective	Dysplasia
LGR5 p53R270/+	NO	p53+/-	0/7
LGR5 p53R270/F	NO	p53+/-	1/5
p53R270/F	YES	p53+/-	0/6
LGR5 p53R270/+	YES	p53+/- Lgr5-R270H/+	1/8
LGR5 p53R270/F	YES	p53+/- Lgr5-R270H/+	1/9

Genotype	Treatment	Effective	Dysplasia
LGR5 p53F/F	none	Lgr5-p53-/-	0/4
LGR5 p53F/F	DCA	Lgr5-p53-/-	0/7
LGR5 p53F/F	MNU	Lgr5-p53-/-	3/4*
LGR5 p53F/F	DCA/MNU	Lgr5-p53-/-	3/5*

*1/6 Cre negative mice treated with DCA/MNU developed dysplasia

Extended Data Fig. 2. Lgr5-p53^{KO} cells have a selective advantage in the setting of dietary carcinogen to promote premalignant gastric lesions

(a) Recombination specific PCR of DNA extract from gastric lesions of Lgr5-p53^{WT} and Lgr5-p53^{KO} mice. Data presented as mean ± s.d of three technical replicates.

(b) Schematic showing Lgr5-p53$^{LSL-R270H}$ experimental design; DCA/MNU treatment and tamoxifen injection schedule during indicated duration depicted below. **(c)** Kaplan-Meier survival curve of Lgr5-p53^{R270H} experiments; table shows frequency of dysplasia in DCA/MNU treated mice of indicated genotype.

(d) Schematic showing Lgr5-p53^{KO} experimental design; DCA alone, MNU alone, or DCA/MNU combination as well as tamoxifen injection schedule during indicated duration depicted below. Table shows frequency of dysplasia in Lgr5-p53^{KO} mice with indicated treatment after 12 months. *1/6 Cre-negative, tamoxifen-induced control mice treated with DCA/MNU developed dysplasia.

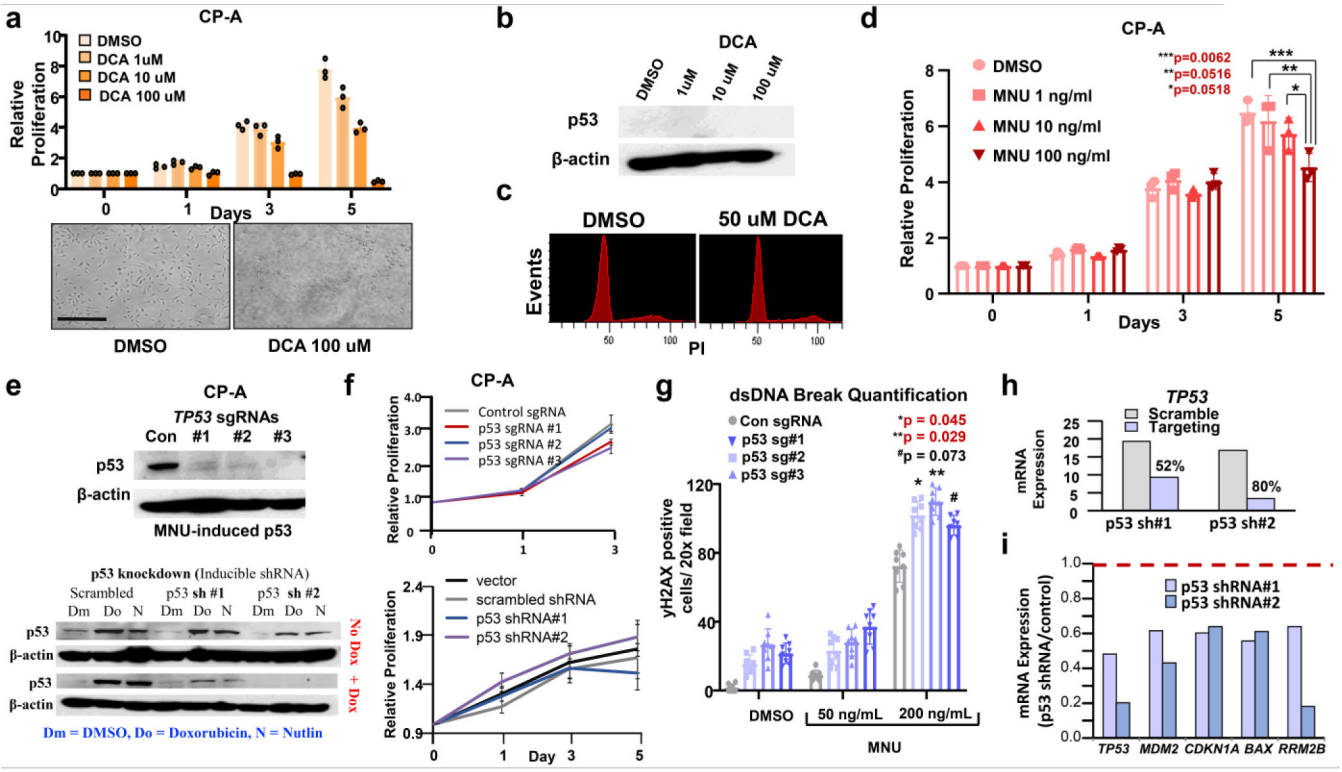

Extended Data Fig. 3. *TP53*-deleted human premalignant cells have a selective growth advantage in the setting of MNU

(a) Relative proliferation of CP-A cells treated with indicated concentrations of DCA; phase contrast images of CP-A cells treated with DMSO or 100μM DCA.

(b) Immunoblot showing protein levels of p53 in CP-A cells treated with DMSO or 50μM DCA. This experiment was repeated once with similar results.

(c) DNA content flow cytometry of CP-A cells expressing control orTP53 shRNA#2 CP-A cells treated with indicated MNU concentrations. This experiment was repeated once with similar results.

(d) Relative proliferation of CP-A cells treated with DMSO or indicated concentrations of MNU by Celltiter Glo. Data presented as mean ± s.d of three culture replicates; p-value calculated by two-sided Student's t-test.

(e) Immunoblot showing protein levels of p53 in genetically modified CP-A cells; top panel shows protein from CP-A cells expressing control sgRNA/Cas9 or three p53 targeting sgRNAs/Cas9 after treatment with MNU 200ng/mL; bottom panel shows protein from CP-A cells expressing a scrambled or two targeting p53 shRNAs treated with DMSO, Doxorubicin, or Nutlin in the presence or absence of doxycycline. This experiment was repeated once.

(f) Relative proliferation of CP-A cells expressing control sgRNA/Cas9 or three p53 targeting sgRNA/Cas9 (top panel); expressing vector control, scramble control, or two p53 targeting shRNAs. Data presented as mean ± s.d of three culture replicates

(g) Quantification of dsDNA breaks in CP-A cells expressing control sgRNA/Cas9 or three p53 targeting sgRNA/Cas9 in the setting of indicated concentrations of MNU by γH2AX

immunofluorescence. Data presented as mean ± s.d of four technical and two cell culture replicates; p-value calculated by two-sided Student's t-test of cell culture replicates.
(h) FPKM gene counts of TP53 in CP-A cells stably expressing two p53 shRNAs
(i) Ratio of TP53 pathway target gene expression levels in CP-A cells expressing indicated p53 shRNA relative to scramble control (cell culture replicates shown)

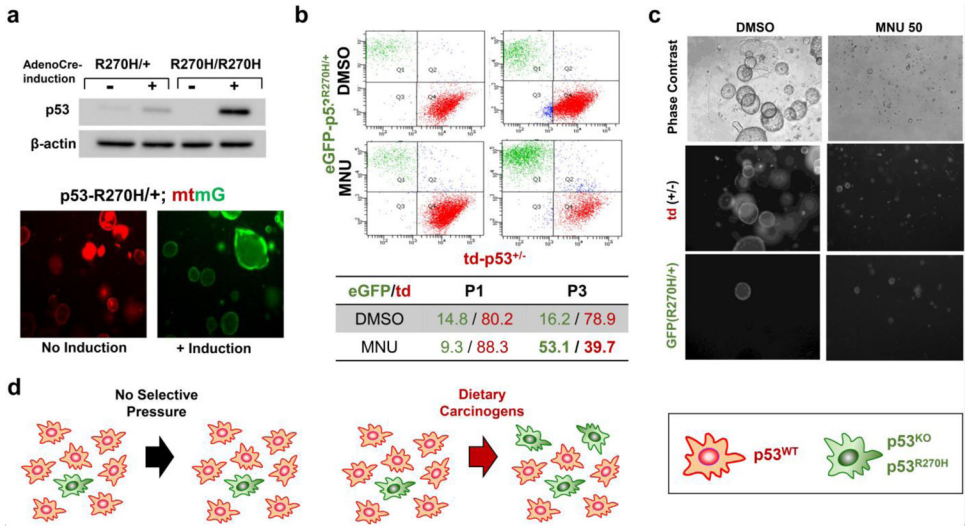

Extended Data Fig. 4. $p53^{R270H/+}$ organoids have a selective growth advantage in the setting of dietary carcinogen exposure.

(a) Immunoblot showing expression of mutant $p53^{R270H}$ in whole cell lysates derived from $p53^{LSL\text{-}R270H/+}$ and $p53^{LSL\text{-}R270H/R270H}$ gastric organoids with or without AdenoCre induction; immunofluorescent images of $p53^{LSL\text{-}R270H/+}$;mtmG gastric organoids before and after AdenoCre induction. Organoids without induction remain red indicating that recombination has not occurred, whereas those with AdenoCre induction convert to green indicating that recombination has occurred. This experiment was repeated once with similar results.

(b) Flow cytometry of eGFP+ Mist-$p53^{R270H/+}$ and td+ Mist-$p53^{+/-}$ organoids cultured in DMSO or 50ng/mL MNU. Quantification of eGFP+ Mist-$p53^{R270H/+}$ and td+ Mist-$p53^{+/-}$ organoids at passage 1 (P1) and 3 (P3).

(c) Phase contrast and immunofluorescent images of eGFP+ Mist-$p53^{R270H/+}$ and td+ Mist-$p53^{+/-}$ organoids cultured in DMSO or 50ng/mL MNU. This experiment was repeated twice with similar results.

(d) Schematic depicting competitive growth advantage of p53-altered gastric organoids in the setting of MNU

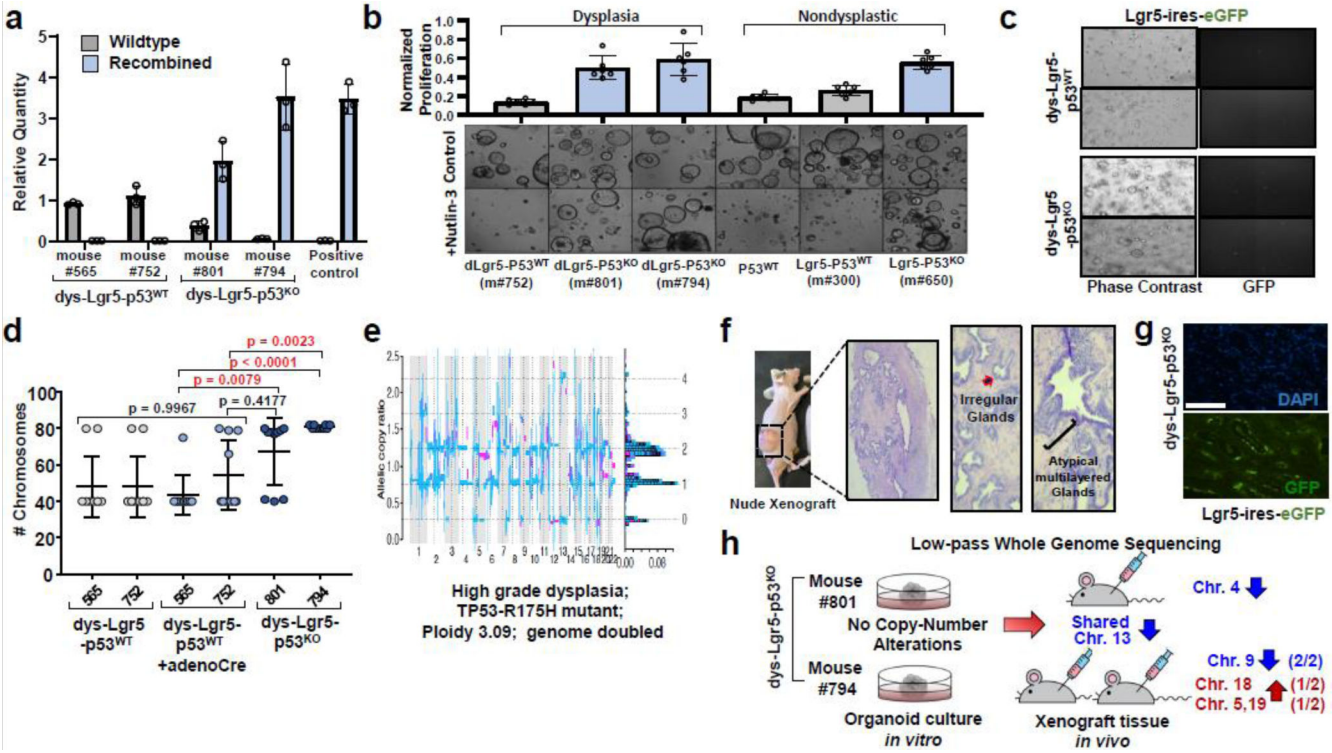

Extended Data Fig. 5. Dysplastic Lgr5-p53^{KO} gastric organoids capture properties of premalignant lesions

(a) Recombination specific PCR of DNA extract from premalignant dys-Lgr5-p53^{WT} and dys-Lgr5-p53^{KO} gastric organoids. Data presented as mean ± s.d of n = 3 technical replicates per group.

(b) Quantification of proliferation by CellTiter-Glo and phase contrast images of nondysplastic and dysplastic Lgr5-p53^{WT} and Lgr5-p53^{KO} gastric organoids in the presence or absence of Nutlin-3 (30uM for 72 hours). Data presented as mean ± s.d. of n = 6 cell culture replicates.

(c) Representative images of phase contrast and GFP-immunofluorescent images from dys-Lgr5-p53^{KO} and dys-Lgr5-p53^{WT} gastric organoid cultures. The experiment was repeated once with similar results.

(d) Karyotype analysis of premalignant Lgr5-p53^{KO} (n = 2 mice), Lgr5-p53^{WT} (n = 2 mice), and Lgr5-p53^{WT} + AdenoCre gastric organoids; chromosome count of 10 cells per group. Data presented as mean ± s.d.; p-values calculated by Ordinary One-way ANOVA with Sidak's multiple comparisons adjustment.

(e) Copy number analysis of a patient specimen of a high-grade dysplastic Barrett's metaplasia harboring *TP53*^{R175H} mutation and genome doubling.

(f) Histopathology of primary tumor xenograft of Lgr5-p53^{KO} gastric organoid showing features of dysplasia. This experiment was repeated twice with similar results.

(g) DAPI staining and GFP (Lgr5+) immunofluorescence of primary xenograft from Lgr5-p53^{KO} gastric organoids. This experiment was repeated twice with similar results.

(h) Schematic of low-pass whole genome sequencing (LP-WGS) experiment of cultured and xenograft dys-Lgr5-p53^{KO} gastric organoids. Common and distinct broad somatic copy number alterations that were only found in xenograft tissue are displayed.

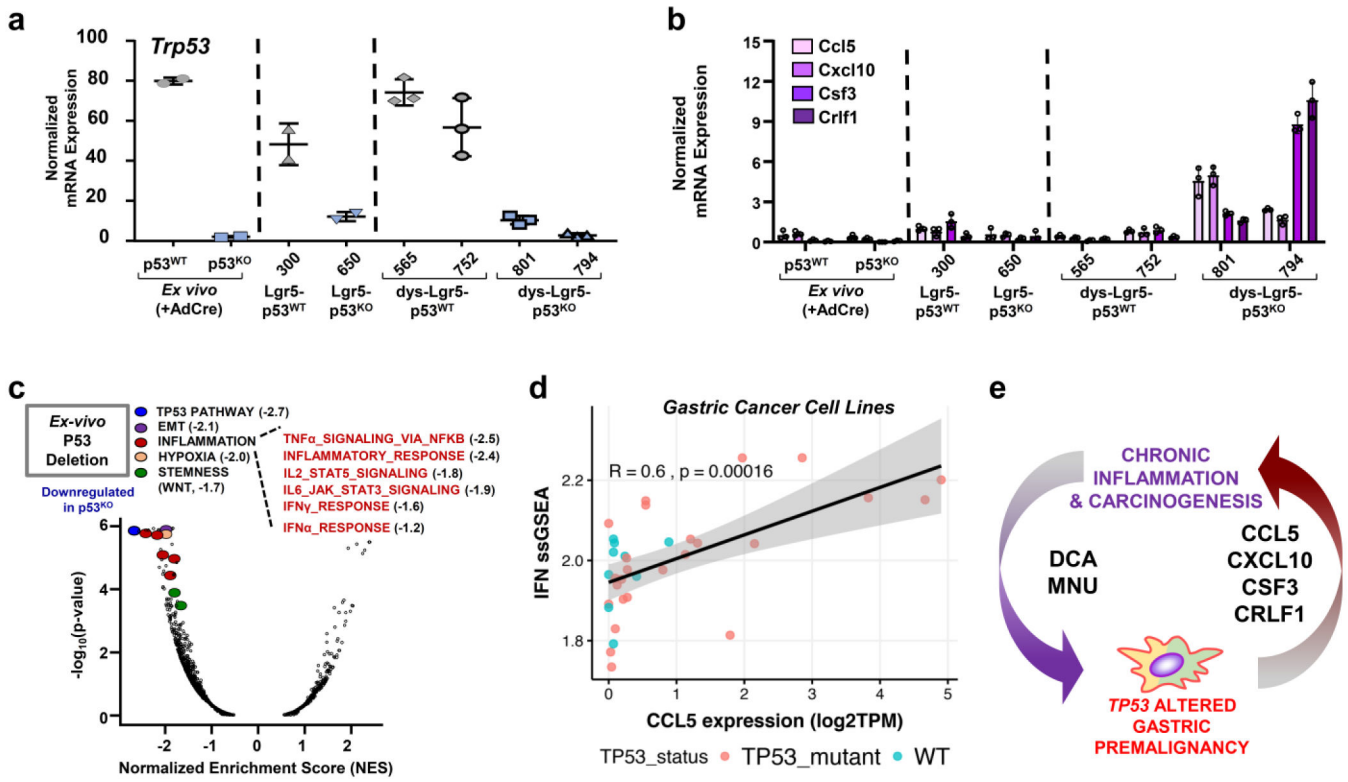

Extended Data Fig. 6. Interferon signaling is upregulated in dysplastic Lgr5-p53^{KO} gastric organoids

(a) mRNA expression of *Trp53* in p53^{KO}, p53^{WT}, Lgr5-p53^{KO}, Lgr5-p53^{WT}, dys-Lgr5-p53^{KO} and dys-Lgr5-p53^{WT} gastric organoids. Data presented as mean ± s.d. of n = 2 (nondysplastic) and n = 3 (dysplastic) cell culture replicates.

(b) mRNA expression levels of *Csf3*, *Cxcl10*, and *Ccl5* in p53^{KO}, p53^{WT}, Lgr5-p53^{KO}, Lgr5-p53^{WT}, dys-Lgr5-p53^{KO} and dys-Lgr5-p53^{WT} gastric organoids by RT-PCR. Data presented as mean ± s.d. of n = 3 cell culture replicates.

(c) Volcano plot of differential expressed gene-sets in p53^{KO} gastric organoids plotted as normalized enrichment scores (NES) by -log10(p-value), where p-values for gene set enrichment scores were determined by randomly permuting genes (n=100,000 permutations). Individual inflammation gene sets are described with corresponding NES.

(d) Scatter plot of single sample GSEA (ssGSEA) of interferon pathway and *Ccl5* mRNA expression in gastric cancer cell lines annotated by *TP53* mutation status (n = 26 for *TP53* mutant and n = 10 for *TP53* wildtype). Gray shaded region represents 95% confidence interval of the linear regression fit. Pearson's correlation value R = 0.6 and p-value computed based on a two-sided t-distribution.

(e) Schematic of proposed vicious feedback cycle in gastric premalignancy: chronic inflammation and carcinogen exposure selects for p53 mutant gastric cells, which in turn stimulate inflammatory cytokines, particularly *Csf3, Cxcl10, Ccl5*

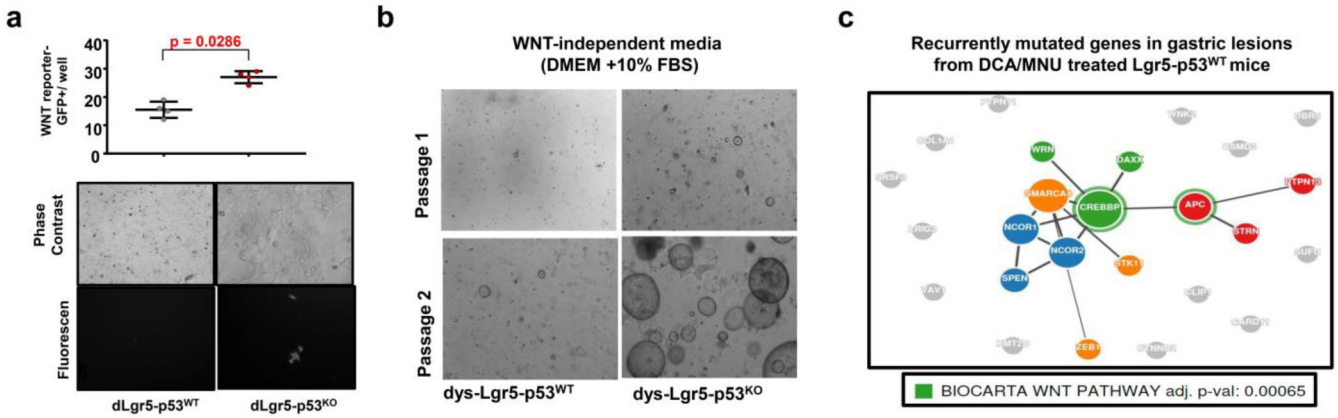

Extended Data Fig. 7. WNT pathway is upregulated in dysplastic Lgr5-p53^{KO} gastric organoids

(a) WNT-reporter activity in adherent culture of dys-Lgr5-p53^{KO} and dys-Lgr5-p53^{WT} gastric cells following transient transfection. Data presented as mean ± s.d. of n = 4 cell culture replicates; p-value calculated by two-sided Mann Whitney test.

(b) Phase contrast images of dys-Lgr5-p53^{KO} and dys-Lgr5-p53^{WT} gastric organoids two days following the first and second passage in WNT independent media (DMEM + 10%FBS). This experiment was repeated twice with similar results.

(c) Gene network of significantly mutated genes in dysplastic gastric lesions from DCA/MNU-treated Lgr5-p53^{WT} mice (n = 8) using GeNets (adjusted p-value = 0.00065 using Bonferroni correction) (Li et al., 2018).

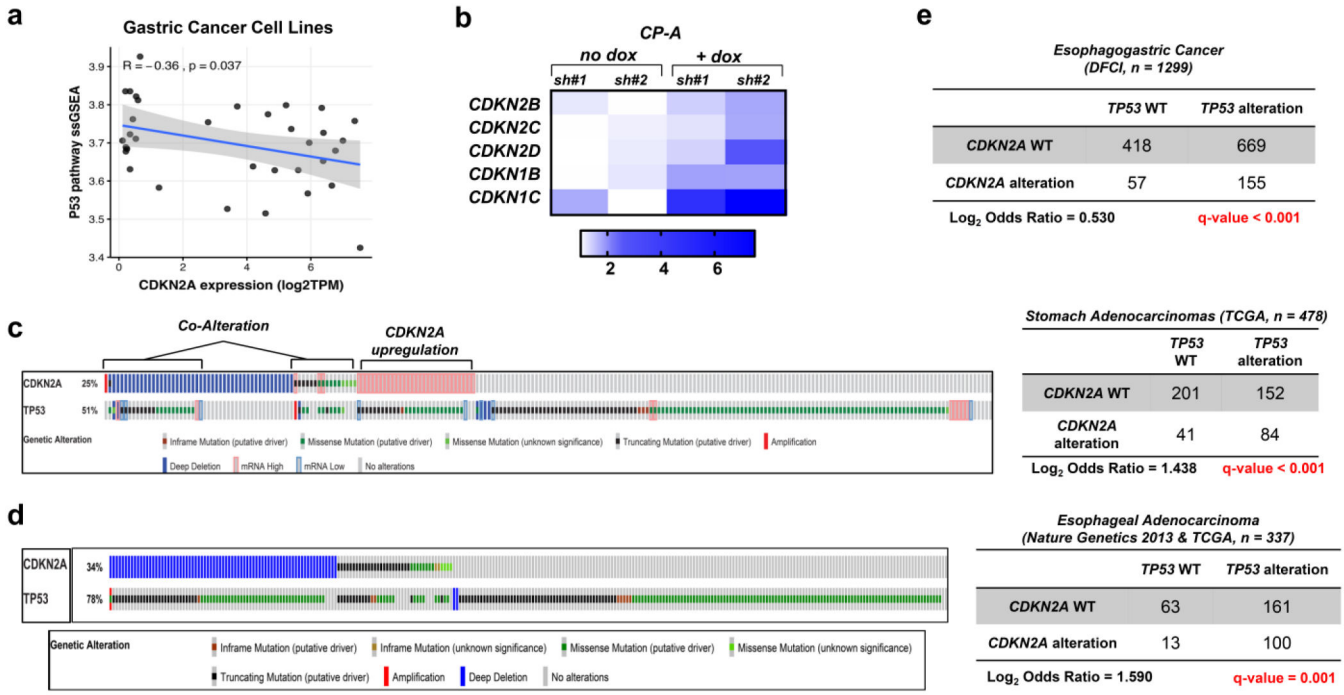

e

Esophagogastric Cancer (DFCI, n = 1299)

	TP53 WT	*TP53* alteration
CDKN2A WT	418	669
CDKN2A alteration	57	155

Log_2 Odds Ratio = 0.530 q-value < 0.001

Stomach Adenocarcinomas (TCGA, n = 478)

	TP53 WT	*TP53* alteration
CDKN2A WT	201	152
CDKN2A alteration	41	84

Log_2 Odds Ratio = 1.438 q-value < 0.001

Esophageal Adenocarcinoma (Nature Genetics 2013 & TCGA, n = 337)

	TP53 WT	*TP53* alteration
CDKN2A WT	63	161
CDKN2A alteration	13	100

Log_2 Odds Ratio = 1.590 q-value = 0.001

Extended Data Fig. 8. *CDKN2A* is upregulated in p53^{KO} premalignant lesions and co-altered with *TP53* in human gastric cancer

(a) Scatter plot of single sample GSEA (ssGSEA) of p53 pathway and *CDKN2A* mRNA expression in gastric cancer cell lines (n = 36). Gray shaded region represents 95% confidence interval of the linear regression fit. Pearson's correlation value R = −0.36 and p-value computed based on a two-sided t-distribution.

(b) Heatmap showing mRNA expression of *CDKN2B, CDKN2C, CDKN2D, CDKN1B, CDKN1C* in CP-A cell line genetically engineered to express two p53 targeting shRNA under doxycycline inducible conditions.

(c) Oncoporint from cbioportal showing alterations and mRNA expression in *CDKN2A* and *TP53* in human gastric adenocarcinomas from TCGA (n = 478). Deep deletions (solid blue); amplifications (solid red); missense mutations in the COSMIC repository (solid green); nonsense or frameshift mutations (black); elevated mRNA expression > 2.0 (hollow red). Table showing number of cases with double, single, or no alteration in *CDKN2A* and *TP53* in human gastric adenocarcinomas from TCGA (right)

(d) Oncoprint from cbioportal showing alterations in *CDKN2A* and *TP53* in human esophageal adenocarcinomas from TCGA and (Dulak et al., 2013) combined data-set (n = 337). Deep deletions (solid blue); amplifications (solid red); missense mutations in the COSMIC repository (solid green); nonsense or frameshift mutations (black). Table showing number of cases with double, single, or no alteration in *CDKN2A* and *TP53* in combined esophageal adenocarcinoma data set.

(e) Table showing number of cases with double, single, or no alteration in *CDKN2A* and *TP53* in combined gastric and esophageal adenocarcinomas from patients treated at DFCI (n = 1299). Q-value determined by one-sided Fischer Exact Test with Benjamin-Hochberg FDR correction.

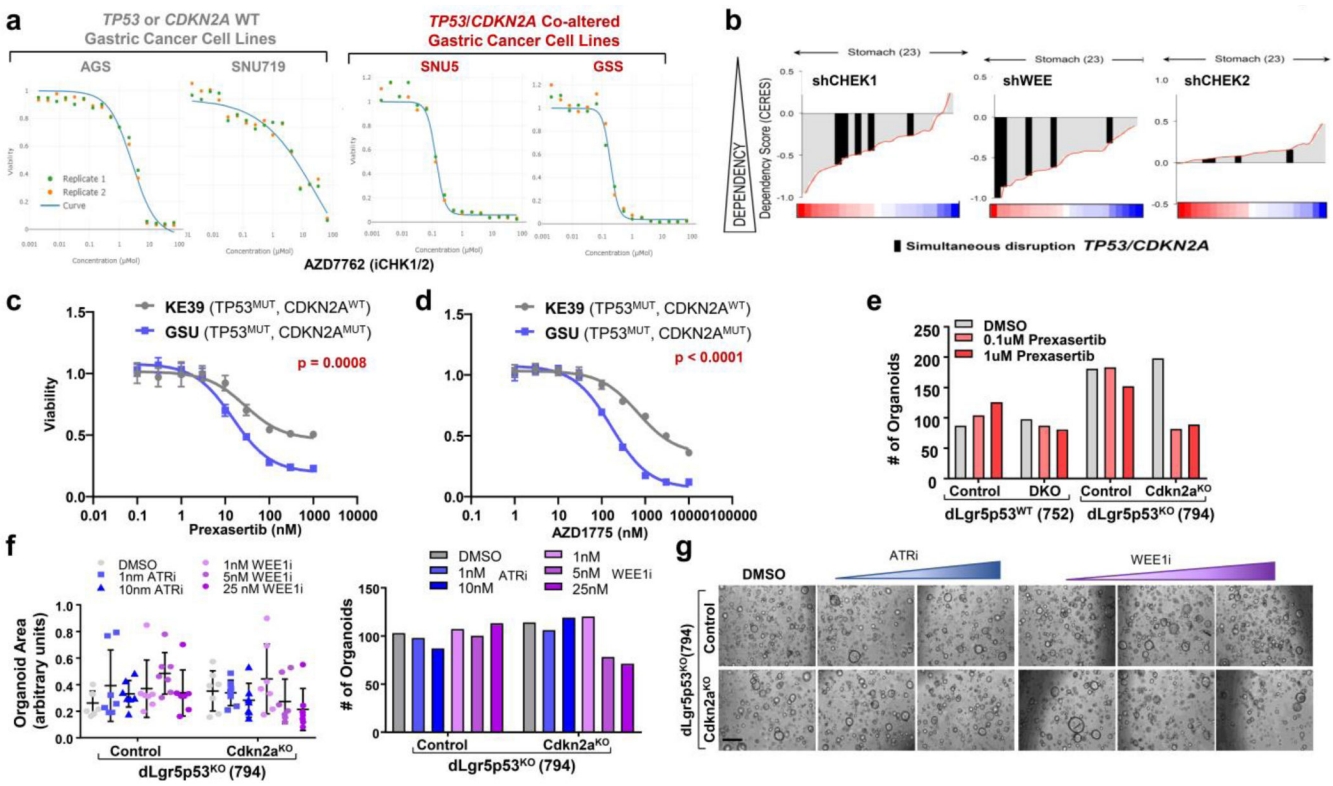

Extended Data Fig. 9. Co-deletion of *CDKN2A* and *TP53* sensitizes to DNA damage response pathway blockade

(a) Dose-response curves of CHK1 inhibitor AZD7762 of two gastric cancer cell lines wildtype for either *TP53* or *CDKN2A* and two gastric cancer cell lines with co-alteration of *TP53* and *CDKN2A*.

(b) Relative dependency of 23 gastric cancer cell lines to CHEK1, CHEK2, and WEE1 shRNA-mediated knockdown as shown by CERES dependency score. Black rectangles indicate gastric cancer cell lines with simultaneous disruption of *TP53* and *CDKN2A*.

(c) Dose-response curve of KE39 ($TP53^{MUT}$, $CDKN2A^{WT}$) and GSU ($TP53^{MUT}$, $CDKN2A^{MUT}$) gastric cancer cell lines to Prexasertib. Data presented as mean ± s.d. of n = 6 cell culture replicates at each dose; p-value calculated by Comparison of Fits based on differences in IC_{50}.

(d) Dose-response curve of KE39 ($TP53^{MUT}$, $CDKN2A^{WT}$) and GSU ($TP53^{MUT}$, $CDKN2A^{MUT}$) gastric cancer cell lines to WEE1 inhibitor AZD1775. Data presented as mean ± s.d. of n = 6 cell culture replicates at each dose; p-value calculated by Comparison of Fits based on differences in IC_{50}.

(e) Quantification by manual counting of number of organoids in experiment from Figure 7f-g.

(f) Quantification of organoid size and number from dys-Lgr5-$p53^{KO}$-control and dys-Lgr5-$p53^{WT}$-$p16^{KO}$ gastric organoids treated for 36 hours with DMSO or indicated concentration of ATR inhibitor AZD6738 or WEE1 inhibitor AZD1775. Data presented as mean ± s.d. of n = 6-8 technical replicates at each dose

(g) Representative phase contrast images from experiment (f)

Supplementary Material

Refer to Web version on PubMed Central for supplementary material.

ACKNOWLEDGEMENTS

We thank Adam Sperling, Manav Korpal, Anil Rustgi, and Shridhar Ganesan for insightful discussions and review of manuscript; Harshabad Singh, Doug Micalizzi, David Liu, and Ankur Nagaraja for insightful discussions; Shumei Wang and the BWH CytoGenomics Core for assistance with karyotype analysis; Aniket Gad and Lay-Hong Ang for assistance with immunohistochemistry and immunofluorescence assays; Dana-Farber/Harvard Cancer Center in Boston, MA, for the use of the Specialized Histopathology Core, which provided histology and immunohistochemistry service; Harvard Digestive Disease Center and NIH grant P30DK034854 for core services, resources, technology, and expertise; Center for Cancer Genome Discovery (CCGD) for their assistance and expertise in whole exome sequencing of murine tissue; Dana-Farber/Harvard Cancer Center is supported in part by an NCI Cancer Center Support Grant # NIH 5 P30 CA06516. This work was funded by grants from the National Cancer Institute P01 CA098101 to A.J.B. and the American Cancer Society Postdoctoral Fellowship, KL2/CMERIT Harvard Catalyst Award, Perry S. Levy Fund for Gastrointestinal Cancer Research, and NIH K08-DK120930 to N.S.S.

REFERENCES

1. Wagner AD et al. Chemotherapy for advanced gastric cancer. Cochrane Database Syst Rev 8, CD004064 (2017). [PubMed: 28850174]
2. Yang K et al. Dietary modulation of carcinoma development in a mouse model for human familial adenomatous polyposis. Cancer Res 58, 5713–7 (1998). [PubMed: 9865728]
3. Polak P et al. Cell-of-origin chromatin organization shapes the mutational landscape of cancer. Nature 518, 360–364 (2015). [PubMed: 25693567]
4. The Cancer Genome Atlas Research Network. Integrated genomic characterization of oesophageal carcinoma. Nature 541, 169–175 (2017). [PubMed: 28052061]
5. Quante M et al. Bile acid and inflammation activate gastric cardia stem cells in a mouse model of Barrett-like metaplasia. Cancer Cell 21, 36–51 (2012). [PubMed: 22264787]
6. Giroux V & Rustgi AK Metaplasia: tissue injury adaptation and a precursor to the dysplasia-cancer sequence. Nat Rev Cancer 17, 594–604 (2017). [PubMed: 28860646]
7. Chen SL, Mo JZ, Cao ZJ, Chen XY & Xiao SD Effects of bile reflux on gastric mucosal lesions in patients with dyspepsia or chronic gastritis. World J Gastroenterol 11, 2834–7 (2005). [PubMed: 15884134]
8. Sobala GM et al. Bile reflux and intestinal metaplasia in gastric mucosa. J Clin Pathol 46, 235–40 (1993). [PubMed: 8463417]
9. Stefaniwsky AB, Tint GS, Speck J, Shefer S & Salen G Ursodeoxycholic acid treatment of bile reflux gastritis. Gastroenterology 89, 1000–4 (1985). [PubMed: 4043659]
10. Tomita H et al. Inhibition of gastric carcinogenesis by the hormone gastrin is mediated by suppression of TFF1 epigenetic silencing. Gastroenterology 140, 879–91 (2011). [PubMed: 21111741]
11. Lijinsky W & Epstein SS Nitrosamines as environmental carcinogens. Nature 225, 21–3 (1970). [PubMed: 5409687]
12. Lijinsky W N-Nitroso compounds in the diet. Mutat Res 443, 129–38 (1999). [PubMed: 10415436]
13. Ding L, El Zaatari M & Merchant JL Recapitulating Human Gastric Cancer Pathogenesis: Experimental Models of Gastric Cancer. Adv Exp Med Biol 908, 441–78 (2016). [PubMed: 27573785]
14. Petersen CP, Mills JC & Goldenring JR Murine Models of Gastric Corpus Preneoplasia. Cell Mol Gastroenterol Hepatol 3, 11–26 (2017). [PubMed: 28174755]
15. Yamachika T et al. N-methyl-N-nitrosourea concentration-dependent, rather than total intake-dependent, induction of adenocarcinomas in the glandular stomach of BALB/c mice. Jpn J Cancer Res 89, 385–91 (1998). [PubMed: 9617343]

16. Fox JG et al. Germ-line p53-targeted disruption inhibits helicobacter-induced premalignant lesions and invasive gastric carcinoma through down-regulation of Th1 proinflammatory responses. Cancer Res 62, 696–702 (2002). [PubMed: 11830522]
17. Wang TC et al. Synergistic interaction between hypergastrinemia and Helicobacter infection in a mouse model of gastric cancer. Gastroenterology 118, 36–47 (2000). [PubMed: 10611152]
18. Wang TC et al. Mice lacking secretory phospholipase A2 show altered apoptosis and differentiation with Helicobacter felis infection. Gastroenterology 114, 675–89 (1998). [PubMed: 9516388]
19. Hayakawa Y et al. Mist1 Expressing Gastric Stem Cells Maintain the Normal and Neoplastic Gastric Epithelium and Are Supported by a Perivascular Stem Cell Niche. Cancer Cell 28, 800–814 (2015). [PubMed: 26585400]
20. Hayakawa Y, Fox JG & Wang TC The Origins of Gastric Cancer From Gastric Stem Cells: Lessons From Mouse Models. Cell Mol Gastroenterol Hepatol 3, 331–338 (2017). [PubMed: 28462375]
21. Sarkar A et al. Sox2 Suppresses Gastric Tumorigenesis in Mice. Cell Rep 16, 1929–41 (2016). [PubMed: 27498859]
22. Leushacke M et al. Lgr5-expressing chief cells drive epithelial regeneration and cancer in the oxyntic stomach. Nat Cell Biol 19, 774–786 (2017). [PubMed: 28581476]
23. Dulak AM et al. Exome and whole-genome sequencing of esophageal adenocarcinoma identifies recurrent driver events and mutational complexity. Nat Genet 45, 478–86 (2013). [PubMed: 23525077]
24. Stachler MD et al. Paired exome analysis of Barrett's esophagus and adenocarcinoma. Nat Genet 47, 1047–55 (2015). [PubMed: 26192918]
25. Zang ZJ et al. Exome sequencing of gastric adenocarcinoma identifies recurrent somatic mutations in cell adhesion and chromatin remodeling genes. Nat Genet 44, 570–4 (2012). [PubMed: 22484628]
26. Sperling AS, Gibson CJ & Ebert BL The genetics of myelodysplastic syndrome: from clonal haematopoiesis to secondary leukaemia. Nat Rev Cancer 17, 5–19 (2017). [PubMed: 27834397]
27. Steensma DP et al. Clonal hematopoiesis of indeterminate potential and its distinction from myelodysplastic syndromes. Blood 126, 9–16 (2015). [PubMed: 25931582]
28. Huang KK et al. Genomic and Epigenomic Profiling of High-Risk Intestinal Metaplasia Reveals Molecular Determinants of Progression to Gastric Cancer. Cancer Cell 33, 137–150 e5 (2018). [PubMed: 29290541]
29. Maley CC et al. Genetic clonal diversity predicts progression to esophageal adenocarcinoma. Nat Genet 38, 468–73 (2006). [PubMed: 16565718]
30. Shimizu T et al. Accumulation of somatic mutations in TP53 in gastric epithelium with Helicobacter pylori infection. Gastroenterology 147, 407–17 e3 (2014). [PubMed: 24786892]
31. Stachler MD et al. Detection of Mutations in Barrett's Esophagus Before Progression to High-Grade Dysplasia or Adenocarcinoma. Gastroenterology (2018).
32. Wang L, Guo H, Lin C, Yang L & Wang X Enrichment and characterization of cancer stemlike cells from a cervical cancer cell line. Mol Med Rep 9, 2117–23 (2014). [PubMed: 24676900]
33. Van de Peer Y, Mizrachi E & Marchal K The evolutionary significance of polyploidy. Nat Rev Genet 18, 411–424 (2017). [PubMed: 28502977]
34. Mirvish SS Role of N-nitroso compounds (NOC) and N-nitrosation in etiology of gastric, esophageal, nasopharyngeal and bladder cancer and contribution to cancer of known exposures to NOC. Cancer Lett 93, 17–48 (1995). [PubMed: 7600541]
35. Bulay O et al. Carcinogenicity test of six nitrosamides and a nitrosocyanamide administered orally to rats. J Natl Cancer Inst 62, 1523–8 (1979). [PubMed: 286123]
36. Tu S et al. Overexpression of interleukin-1beta induces gastric inflammation and cancer and mobilizes myeloid-derived suppressor cells in mice. Cancer Cell 14, 408–19 (2008). [PubMed: 18977329]
37. Westcott PM et al. The mutational landscapes of genetic and chemical models of Kras-driven lung cancer. Nature 517, 489–92 (2015). [PubMed: 25363767]

38. Barker N et al. Lgr5(+ve) stem cells drive self-renewal in the stomach and build long-lived gastric units in vitro. Cell Stem Cell 6, 25–36 (2010). [PubMed: 20085740]
39. Goldenring JR, Nam KT & Mills JC The origin of pre-neoplastic metaplasia in the stomach: chief cells emerge from the Mist. Exp Cell Res 317, 2759–64 (2011). [PubMed: 21907708]
40. Bielski CM et al. Genome doubling shapes the evolution and prognosis of advanced cancers. Nat Genet 50, 1189–1195 (2018). [PubMed: 30013179]
41. Taylor AM et al. Genomic and Functional Approaches to Understanding Cancer Aneuploidy. Cancer Cell 33, 676–689 e3 (2018). [PubMed: 29622463]
42. Cancer Genome Atlas Research, N. Comprehensive molecular characterization of gastric adenocarcinoma. Nature 513, 202–9 (2014). [PubMed: 25079317]
43. Liu Y et al. Comparative Molecular Analysis of Gastrointestinal Adenocarcinomas. Cancer Cell 33, 721–735 e8 (2018). [PubMed: 29622466]
44. Galipeau PC et al. 17p (p53) allelic losses, 4N (G2/tetraploid) populations, and progression to aneuploidy in Barrett's esophagus. Proc Natl Acad Sci U S A 93, 7081–4 (1996). [PubMed: 8692948]
45. Galipeau PC, Prevo LJ, Sanchez CA, Longton GM & Reid BJ Clonal expansion and loss of heterozygosity at chromosomes 9p and 17p in premalignant esophageal (Barrett's) tissue. J Natl Cancer Inst 91, 2087–95 (1999). [PubMed: 10601379]
46. Nanki K et al. Divergent Routes toward Wnt and R-spondin Niche Independency during Human Gastric Carcinogenesis. Cell 174, 856–869 e17 (2018). [PubMed: 30096312]
47. Cancer Genome Atlas Research, N. et al. Integrated genomic characterization of oesophageal carcinoma. Nature 541, 169–175 (2017). [PubMed: 28052061]
48. Ross-Innes CS et al. Whole-genome sequencing provides new insights into the clonal architecture of Barrett's esophagus and esophageal adenocarcinoma. Nat Genet 47, 1038–46 (2015). [PubMed: 26192915]
49. Jaenisch R & Young R Stem cells, the molecular circuitry of pluripotency and nuclear reprogramming. Cell 132, 567–82 (2008). [PubMed: 18295576]
50. Yaeger R et al. Genomic Alterations Observed in Colitis-Associated Cancers Are Distinct From Those Found in Sporadic Colorectal Cancers and Vary by Type of Inflammatory Bowel Disease. Gastroenterology 151, 278–287 e6 (2016). [PubMed: 27063727]
51. Sharpless NE & DePinho RA The INK4A/ARF locus and its two gene products. Curr Opin Genet Dev 9, 22–30 (1999). [PubMed: 10072356]
52. Chin L et al. Cooperative effects of INK4a and ras in melanoma susceptibility in vivo. Genes Dev 11, 2822–34 (1997). [PubMed: 9353252]
53. Kamijo T et al. Functional and physical interactions of the ARF tumor suppressor with p53 and Mdm2. Proc Natl Acad Sci U S A 95, 8292–7 (1998). [PubMed: 9653180]
54. Pomerantz J et al. The Ink4a tumor suppressor gene product, p19Arf, interacts with MDM2 and neutralizes MDM2's inhibition of p53. Cell 92, 713–23 (1998). [PubMed: 9529248]
55. Stott FJ et al. The alternative product from the human CDKN2A locus, p14(ARF), participates in a regulatory feedback loop with p53 and MDM2. EMBO J 17, 5001–14 (1998). [PubMed: 9724636]
56. Zhang Y, Xiong Y & Yarbrough WG ARF promotes MDM2 degradation and stabilizes p53: ARF-INK4a locus deletion impairs both the Rb and p53 tumor suppression pathways. Cell 92, 725–34 (1998). [PubMed: 9529249]
57. Lukas J et al. Retinoblastoma-protein-dependent cell-cycle inhibition by the tumour suppressor p16. Nature 375, 503–6 (1995). [PubMed: 7777060]
58. Otterson GA, Kratzke RA, Coxon A, Kim YW & Kaye FJ Absence of p16INK4 protein is restricted to the subset of lung cancer lines that retains wildtype RB. Oncogene 9, 3375–8 (1994). [PubMed: 7936665]
59. Russo AA, Tong L, Lee JO, Jeffrey PD & Pavletich NP Structural basis for inhibition of the cyclin-dependent kinase Cdk6 by the tumour suppressor p16INK4a. Nature 395, 237–43 (1998). [PubMed: 9751050]
60. Shapiro GI et al. Reciprocal Rb inactivation and p16INK4 expression in primary lung cancers and cell lines. Cancer Res 55, 505–9 (1995). [PubMed: 7834618]

61. Tanaka H et al. Disruption of the RB pathway and cell-proliferative activity in non-small-cell lung cancers. Int J Cancer 79, 111–5 (1998). [PubMed: 9583722]
62. Maley CC et al. The combination of genetic instability and clonal expansion predicts progression to esophageal adenocarcinoma. Cancer Res 64, 7629–33 (2004). [PubMed: 15492292]
63. Maley CC et al. Selectively advantageous mutations and hitchhikers in neoplasms: p16 lesions are selected in Barrett's esophagus. Cancer Res 64, 3414–27 (2004). [PubMed: 15150093]
64. Buas MF et al. Integrative post-genome-wide association analysis of CDKN2A and TP53 SNPs and risk of esophageal adenocarcinoma. Carcinogenesis 35, 2740–7 (2014). [PubMed: 25280564]
65. Ku SY et al. Rb1 and Trp53 cooperate to suppress prostate cancer lineage plasticity, metastasis, and antiandrogen resistance. Science 355, 78–83 (2017). [PubMed: 28059767]
66. Mu P et al. SOX2 promotes lineage plasticity and antiandrogen resistance in TP53- and RB1-deficient prostate cancer. Science 355, 84–88 (2017). [PubMed: 28059768]
67. Shapiro GI, Edwards CD, Ewen ME & Rollins BJ p16INK4A participates in a G1 arrest checkpoint in response to DNA damage. Mol Cell Biol 18, 378–87 (1998). [PubMed: 9418885]
68. Bartkova J et al. DNA damage response as a candidate anti-cancer barrier in early human tumorigenesis. Nature 434, 864–70 (2005). [PubMed: 15829956]
69. Gorgoulis VG et al. Activation of the DNA damage checkpoint and genomic instability in human precancerous lesions. Nature 434, 907–13 (2005). [PubMed: 15829965]
70. Chen Z et al. Selective Chk1 inhibitors differentially sensitize p53-deficient cancer cells to cancer therapeutics. Int J Cancer 119, 2784–94 (2006). [PubMed: 17019715]
71. Reaper PM et al. Selective killing of ATM- or p53-deficient cancer cells through inhibition of ATR. Nat Chem Biol 7, 428–30 (2011). [PubMed: 21490603]
72. Gadhikar MA et al. CDKN2A/p16 Deletion in Head and Neck Cancer Cells Is Associated with CDK2 Activation, Replication Stress, and Vulnerability to CHK1 Inhibition. Cancer Res 78, 781–797 (2018). [PubMed: 29229598]
73. Cerami E et al. The cBio cancer genomics portal: an open platform for exploring multidimensional cancer genomics data. Cancer Discov 2, 401–4 (2012). [PubMed: 22588877]
74. Lv L et al. Tetraploid cells from cytokinesis failure induce aneuploidy and spontaneous transformation of mouse ovarian surface epithelial cells. Cell Cycle 11, 2864–75 (2012). [PubMed: 22801546]
75. Shi G et al. Loss of the acinar-restricted transcription factor Mist1 accelerates Kras-induced pancreatic intraepithelial neoplasia. Gastroenterology 136, 1368–78 (2009). [PubMed: 19249398]
76. Shalem O et al. Genome-scale CRISPR-Cas9 knockout screening in human cells. Science 343, 84–87 (2014). [PubMed: 24336571]
77. Sanjana NE, Shalem O & Zhang F Improved vectors and genome-wide libraries for CRISPR screening. Nat Methods 11, 783–784 (2014). [PubMed: 25075903]
78. Wong GS et al. Targeting wild-type KRAS-amplified gastroesophageal cancer through combined MEK and SHP2 inhibition. Nat Med 24, 968–977 (2018). [PubMed: 29808010]
79. Li H & Durbin R Fast and accurate short read alignment with Burrows-Wheeler transform. Bioinformatics 25, 1754–60 (2009). [PubMed: 19451168]
80. McKenna A et al. The Genome Analysis Toolkit: a MapReduce framework for analyzing next-generation DNA sequencing data. Genome Res 20, 1297–303 (2010). [PubMed: 20644199]
81. Cibulskis K et al. Sensitive detection of somatic point mutations in impure and heterogeneous cancer samples. Nat Biotechnol 31, 213–9 (2013). [PubMed: 23396013]
82. Wang K, Li M & Hakonarson H ANNOVAR: functional annotation of genetic variants from high-throughput sequencing data. Nucleic Acids Res 38, e164 (2010). [PubMed: 20601685]
83. Kim J et al. Somatic ERCC2 mutations are associated with a distinct genomic signature in urothelial tumors. Nat Genet 48, 600–606 (2016). [PubMed: 27111033]
84. Boeva V et al. Control-FREEC: a tool for assessing copy number and allelic content using next-generation sequencing data. Bioinformatics 28, 423–5 (2012). [PubMed: 22155870]
85. Scheinin I et al. DNA copy number analysis of fresh and formalin-fixed specimens by shallow whole-genome sequencing with identification and exclusion of problematic regions in the genome assembly. Genome Res 24, 2022–32 (2014). [PubMed: 25236618]

86. Robinson MD & Oshlack A A scaling normalization method for differential expression analysis of RNA-seq data. Genome Biol 11, R25 (2010). [PubMed: 20196867]

87. Robinson MD, McCarthy DJ & Smyth GK edgeR: a Bioconductor package for differential expression analysis of digital gene expression data. Bioinformatics 26, 139–40 (2010). [PubMed: 19910308]

88. Ritchie ME et al. limma powers differential expression analyses for RNA-sequencing and microarray studies. Nucleic Acids Res 43, e47 (2015). [PubMed: 25605792]

89. Law CW, Chen Y, Shi W & Smyth GK voom: Precision weights unlock linear model analysis tools for RNA-seq read counts. Genome Biol 15, R29 (2014). [PubMed: 24485249]

90. Benjamini Y, Drai D, Elmer G, Kafkafi N & Golani I Controlling the false discovery rate in behavior genetics research. Behav Brain Res 125, 279–84 (2001). [PubMed: 11682119]

91. Subramanian A et al. Gene set enrichment analysis: a knowledge-based approach for interpreting genome-wide expression profiles. Proc Natl Acad Sci U S A 102, 15545–50 (2005). [PubMed: 16199517]

92. Sergushichev AA et al. GAM: a web-service for integrated transcriptional and metabolic network analysis. Nucleic Acids Res 44, W194–200 (2016). [PubMed: 27098040]

93. Liberzon A et al. The Molecular Signatures Database (MSigDB) hallmark gene set collection. Cell Syst 1, 417–425 (2015). [PubMed: 26771021]

94. Barbie DA et al. Systematic RNA interference reveals that oncogenic KRAS-driven cancers require TBK1. Nature 462, 108–12 (2009). [PubMed: 19847166]

95. Hanzelmann S, Castelo R & Guinney J GSVA: gene set variation analysis for microarray and RNA-seq data. BMC Bioinformatics 14, 7 (2013). [PubMed: 23323831]

96. Barretina J et al. The Cancer Cell Line Encyclopedia enables predictive modelling of anticancer drug sensitivity. Nature 483, 603–7 (2012). [PubMed: 22460905]

97. Seashore-Ludlow B et al. Harnessing Connectivity in a Large-Scale Small-Molecule Sensitivity Dataset. Cancer Discov 5, 1210–23 (2015). [PubMed: 26482930]

98. Cowley GS et al. Parallel genome-scale loss of function screens in 216 cancer cell lines for the identification of context-specific genetic dependencies. Sci Data 1, 140035 (2014). [PubMed: 25984343]

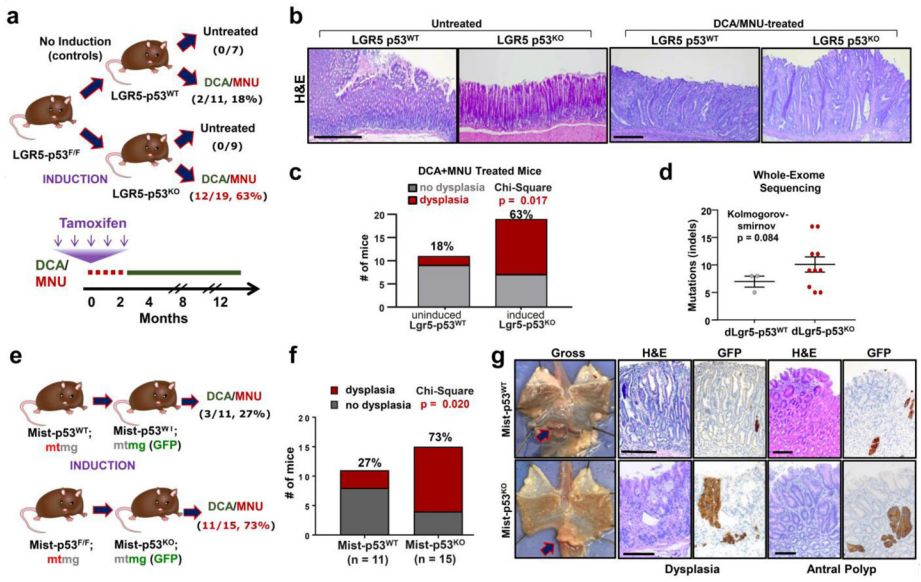

Figure 1. Lgr5-p53^{KO} promotes dysplastic and metaplastic premalignant lesions in the setting of dietary carcinogen exposure.

(a) Schematic showing Lgr5-p53 experimental design and outcomes; percentages represent frequency of mice with antral dysplastic lesions. DCA/MNU treatment and tamoxifen injection schedule indicated on schematic below.

(b) Representative H&E staining of gastric lesions from untreated and DCA/MNU treated Lgr5-p53 mice. Scale bar = 250μM.

(c) Quantification of frequency of dysplasia in mice at 12 months in DCA/MNU treated Lgr5-p53^{WT} (n = 11) and Lgr5-p53^{KO} (n = 19) mice. This experiment was repeated once with similar results.

(d) Mutation burden in the form of insertions and deletions (indels) in dysplastic gastric lesions from Lgr5-p53^{WT} (n = 3) and Lgr5-p53^{KO} (n = 10) mice using whole-exome sequencing. Data is presented as mean ± s.e.m.; two-sided Kolmogorov-smirnov p = 0.084.

(e) Schematic showing Mist-p53;mtmg experimental design and outcomes; percentages represent frequency of dysplastic lesions found in the antrum or corpus of mice. Same DCA/MNU treatment and tamoxifen injection schedule as shown in (a)

(f) Quantification of mice with antral or corpus dysplasia in DCA/MNU treated Mist-p53^{WT} (n = 11) and Mist-p53^{KO} (n = 15) mice at 12 months. This experiment was performed once.

(g) Representative images from DCA/MNU-treated Mist-p53^{WT} and Mist-p53^{KO} mice. Dissection microscope images of lower esophagus and stomach flayed open along greater curvature; arrow indicates antral lesion (left panel). H&E staining and GFP immunohistochemistry of regions of dysplasia and antral polyps. Scale bar = 125μM.

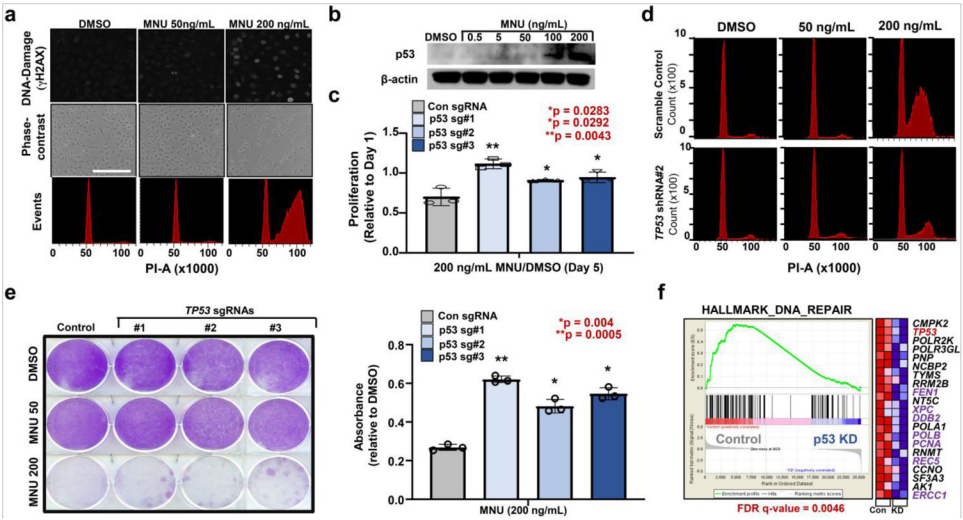

Figure 2. p53^{KO} human nondysplastic premalignant cells have a selective advantage in the setting of MNU exposure

(a) dsDNA damage as indicated by γH2Ax immunofluorescence (top panel), phase-contrast microscopy (middle panel) and DNA content flow cytometry (bottom panel) of CP-A cells treated with indicated doses of MNU. This experiment was repeated three times.

(b) Immunoblot showing protein levels of p53 in CP-A cells treated with DMSO or indicated concentrations of MNU. This experiment was repeated three times.

(c) Relative proliferation of control (n = 3) or p53 KO CP-A cells (n = 3/sgRNA) treated with MNU by Celtiter glo assay. Data presented as mean ± s.d.; p-values calculated by two-sided Student's t-test.

(d) DNA content flow cytometry of CP-A cells expressing control orTP53 shRNA#2 CP-A cells treated with indicated MNU concentrations

(e) Colony formation of CP-A cells stably expressing control or p53 targeting sgRNAs/Cas9 treated with indicated MNU concentrations (left). Quantification of colony formation assay using acetic acid treatment and subsequent absorbance measurement (right). Data presented as mean ± s.d. of three culture replicates p-value calculaged byusing two-sided Student's t-test.

(f) Gene set enrichment analysis showing relative enrichment of DNA repair pathway in control (n = 2) and p53^{KD} CP-A cells (n = 4) (Fasle Discovery Rate q-value = 0.0046). Genes associated with DNA repair are indicated in purple.

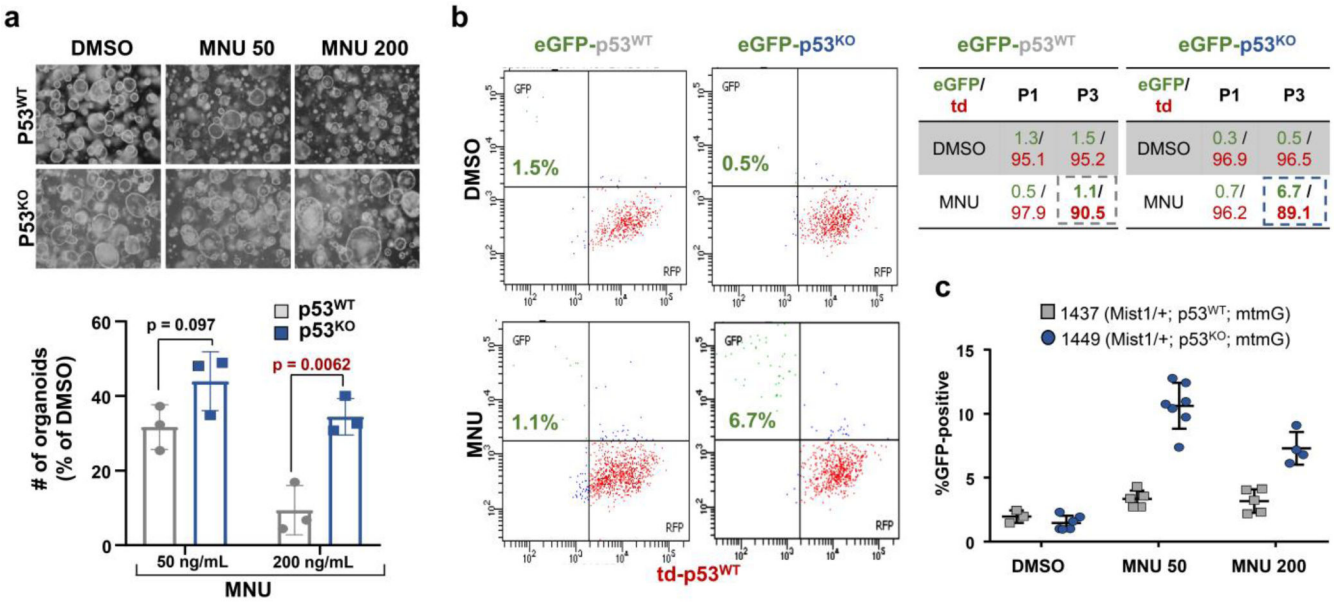

Figure 3. p53^{KO} murine gastric organoids have a competitive advantage in the setting of dietary carcinogenesis

(a) Phase contrast images and quantification of p53^{WT} and p53^{KO} organoids in the setting of DMSO, 50ng/mL MNU, or 200ng/mL MNU (n = 3/group). Data presented as mean ± s.d. of three culture replicates; p-values calculated by two-sided Student's t-test. **(b)** Flow cytometry of GFP+ Mist-p53^{WT} and GFP+ Mist-p53^{KO} relative to RFP+ p53^{WT} organoids cultured in DMSO or 50ng/mL MNU. Quantification of GFP+ Mist-p53^{WT}, GFP+ Mist-p53^{KO} , and RFP+ p53^{WT} organoids at passage 1 (P1) and 3 (P3). The experiment was repeated once.

(c) Quantification of percent GFP+ Mist-p53^{WT} (mouse #1437) and GFP+ Mist-p53^{KO} (mouse #1449) relative to RFP+ p53^{WT} organoids cultured in DMSO, 50ng/mL MNU, or 200ng/mL MNU. There are between 5-7 cell culture replicates per condition.

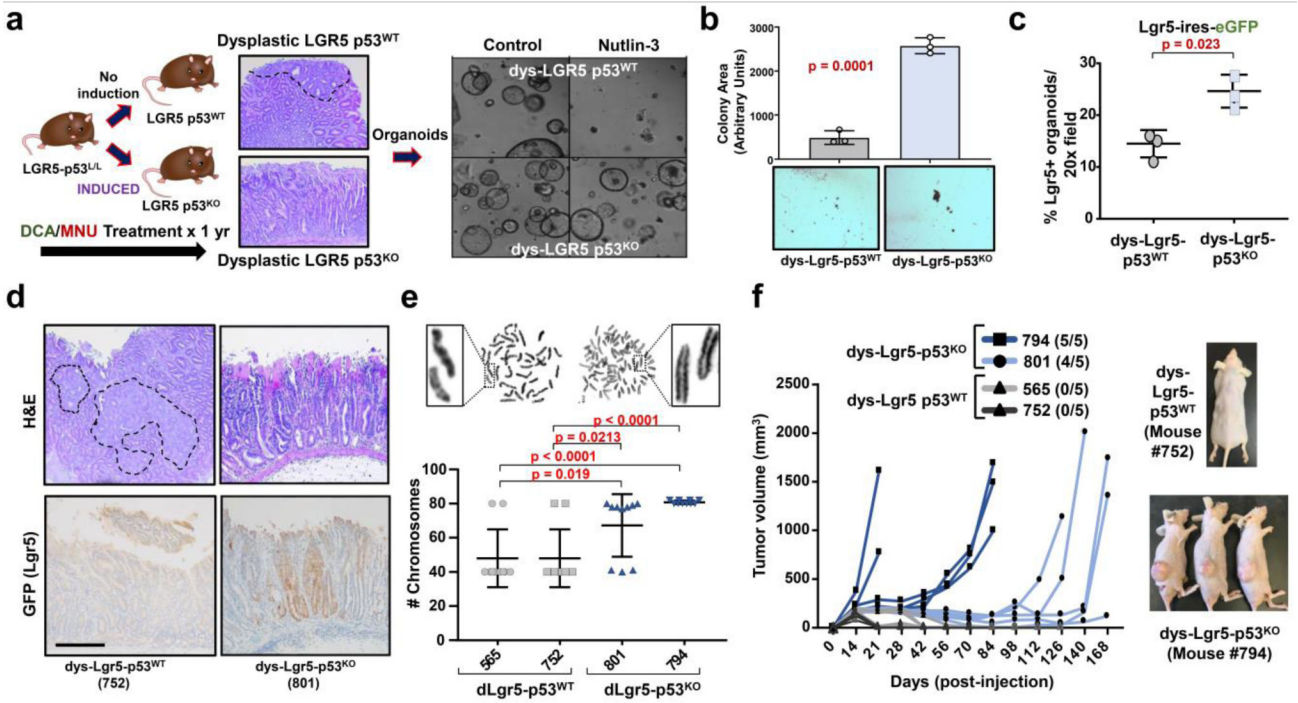

Figure 4. Dysplastic and metaplastic Lgr5-p53^{KO} gastric organoids demonstrate genome doubling and capacity to transform

(a) Schematic showing isolation of dysplastic organoids from premalignant dys-Lgr5-p53^{KO} and dys-Lgr5-p53^{WT} gastric organoids from experiments shown in Figure 1. Phase contrast images of Nutlin-3 treated dys-Lgr5-p53^{KO} and dys-Lgr5-p53^{WT} gastric organoids

(b) Quantification of colony forming ability in ultra-low attachment culture of dys-Lgr5-p53^{KO} and dys-Lgr5-p53^{WT} gastric organoids. Data presented as mean ± s.d. from three biological replicates; p-values calculated by two-sided Student's t-test.

(c) Quantification of percent Lgr5+ cells in dys-Lgr5-p53^{KO} and dys-Lgr5-p53^{WT} gastric organoid culture as measured by GFP+. Data presented as mean ± s.d. from three biological replicates; p-values calculated by two-sided Student's t-test.

(d) Histopathological analysis of gastric dysplasia in dys-Lgr5-p53^{KO} and dys-Lgr5-p53^{WT} mice: H&E stain (top), Alcian blue stain (middle), anti-GFP/Lgr5 IHC (bottom)

(e) Karyotype analysis of dys-Lgr5-p53^{KO} (n = 2 mice) and dys-Lgr5-p53^{WT} (n = 2 mice) gastric organoids; chromosome count of 10 cells per group. Representative images shown to the right; inserts are higher magnification images of chromosomes. Data presented as mean ± s.e.m.; p-values calculated by two-sided Student's t-test.

(f) Primary xenograft growth of dys-Lgr5-p53^{KO} (n = 10 mice) and dys-Lgr5-p53^{WT} (n = 10 mice) gastric organoids in nude mice

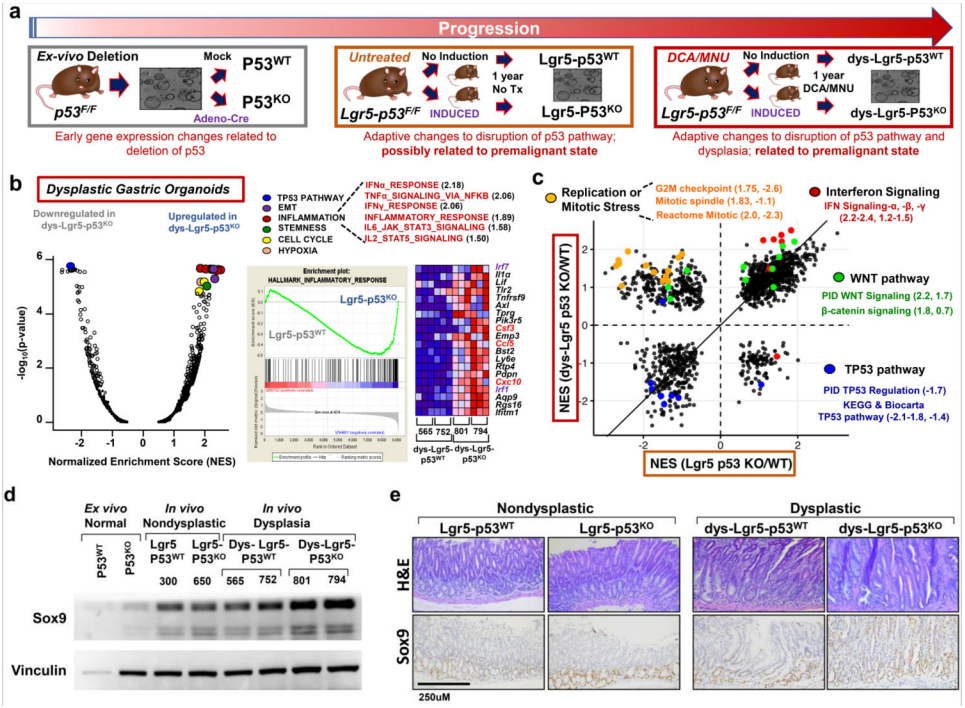

Figure 5. Dysregulation of inflammatory, stem cell, and cell cycle pathways in dysplastic Lgr5-p53^{KO} gastric organoids

(a) Schematic showing methodology for gene expression profiling of p53^{KO}(n = 2), p53^{WT}(n = 2), Lgr5-p53^{KO} (n = 2), Lgr5-p53^{WT} (n = 2), dys-Lgr5-p53^{KO} (n = 6) and dys-Lgr5-p53^{WT} (n = 6) gastric organoids.

(b) Volcano plot of gene-set enrichment pathways in premalignant dLgr5-p53^{KO} (n = 5 organoids from 2 mice) versus dLgr5-p53^{WT} (n = 6 organoids from 2 mice) gastric organoids plotted as normalized enrichment scores (NES) by -log10(p-value), where p-values for gene set enrichment scores were determined by randomly permuting genes (n=100,000 permutations) (left). Individual inflammation gene sets are described with corresponding Normalized Enrichment Scores (NES). Gene-set enrichment plot of *inflammatory response pathway*; associated heat map of scoring genes in gene-set (right).

(c) Scatter plot of NES of gene-sets in dys-Lgr5-p53^{KO}/dys-Lgr5-p53^{WT} (y-axis) versus nondysplastic Lgr5-p53^{KO}/Lgr5-p53^{WT} (x-axis) gastric organoids; Select pathways downregulated in both comparisons are indicated in blue; upregulated in both comparisons indicated in red; and only upregulated in dys-Lgr5-p53^{KO} comparison indicated in orange.

(d) Immunoblot showing protein levels of WNT target Sox9, total β-catenin, and vinculin (loading control) in p53^{WT}, p53^{KO} , Lgr5-p53^{WT}, Lgr5-p53^{KO}, dys-Lgr5-p53^{WT}, dys-Lgr5-p53^{KO} gastric organoids. This experiment was repeated once.

(e) Histopathology of nondysplastic gastric antrum of untreated Lgr5-p53^{WT} and Lgr5-p53^{KO} mice and dysplastic gastric lesions from treated dys-Lgr5-p53^{WT} and dys-Lgr5-p53^{KO} mice; H&E staining (top panel) and Sox9 immunohistochemistry (bottom panel) of gastric antrum. Scale bar = 250μM

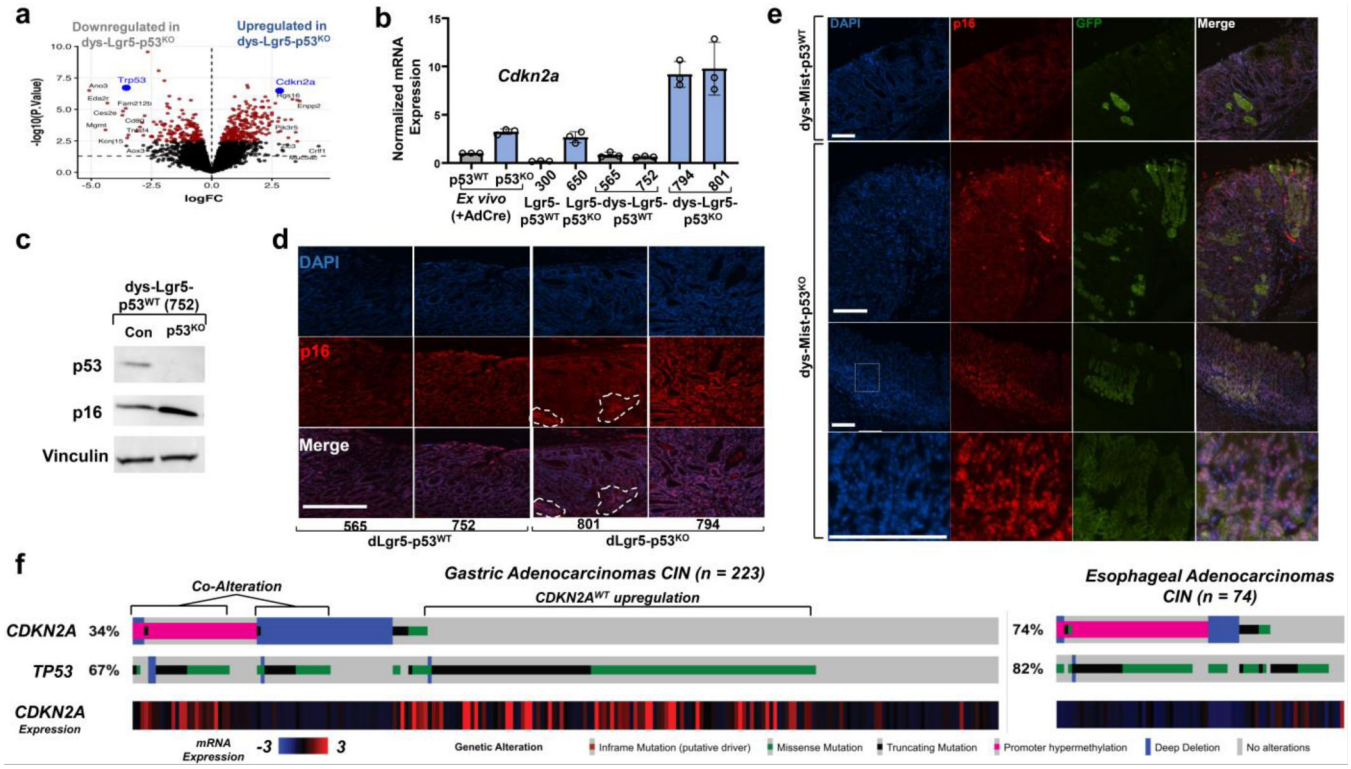

Figure 6. *CDKN2A*/p16 is upregulated in Lgr5-p53^{KO} premalignant gastric lesions and co-altered with *TP53* in a subset of human gastric cancers

(a) Volcano plot of differentially expressed genes in dys-Lgr5-p53^{KO} (n = 6, three cell culture replicates from 2 different mice) relative to dys-Lgr5-p53^{WT} (n = 6, three cell culture replicates from 2 different mice) gastric organoids show as log fold-change (logFC, x-axis) by -$\log_{10}$(p-value), where p-values were estimated from empirical-Bayes moderated t-statistics. Dots colored red have FDR < 0.1, where FDR-adjusted p-values are estimated using the Benjamini-Hochberg method.

(b) mRNA expression of *CDKN2A* in p53^{WT}, p53^{KO}, Lgr5-p53^{WT}, Lgr5-p53^{KO}, dys-Lgr5-p53^{WT} and dys-Lgr5-p53^{KO} gastric organoids

(c) Immunoblot showing protein levels of p53, p16, and vinculin (loading control) in dys-Lgr5-p53^{WT} expressing either a control sgRNA or Trp53 sgRNA. This experiment was repeated once.

(d) Localization and expression levels of p16 (red) in dysplastic lesions of DCA/MNU-treated Lgr5-p53^{WT} and Lgr5-p53^{KO} mice. Nuclear staining by DAPI (blue). Scale bar = 125μM

(e) Localization and expression levels of p16 (red) in dysplastic lesions of DCA/MNU-treated Mist-p53^{WT} and Mist-p53^{KO} mice. GFP+ represents conditionally induced Mist+ cells in indicated genetic mice. Nuclear staining by DAPI (blue). Scale bar = 125μM

(f) Oncoprint from cbioportal[73] showing alterations in *CDKN2A* and *TP53* as well as *CDKN2A* mRNA expression levels in the CIN-subtype of human gastric (n = 223) and esophageal (n = 74) adenocarcinomas from TCGA. Deep deletions (solid blue); missense mutations in the COSMIC repository (solid green); nonsense or frameshift mutations

(black); promoter methylation (magenta). *CDKN2A* mRNA expression from Z-scores of −3 to 3.

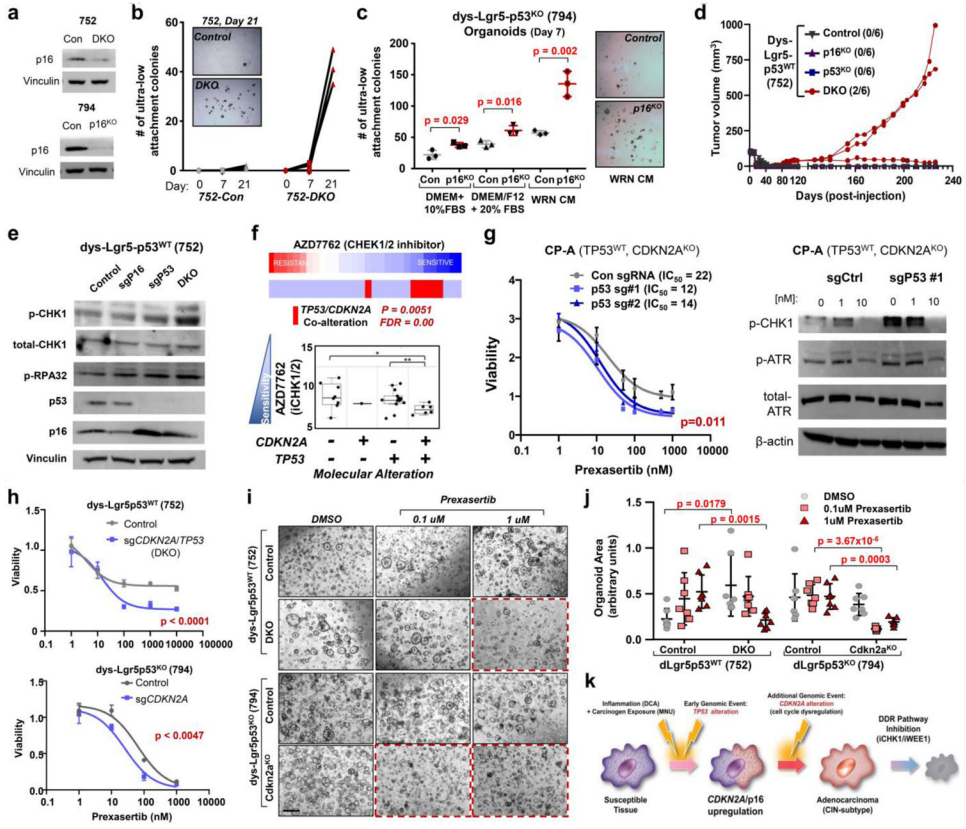

Figure 7. Co-deletion of *CDKN2A*/p16 and *TP53* promotes gastric premalignancy, induces replication stress, and sensitizes to DNA damage response pathway blockade

(a) Immunoblot showing protein levels of p53, p16, and vinculin (loading control) in dys-Lgr5-p53^{WT} control or Trp53/Cdkn2a DKO (top panel) and dys-Lgr5-p53^{KO} control or p16 KO gastric organoids. This experiment was repeated once.

(b) Quantification and representative dissection microscope images of dys-Lgr5-p53^{WT} control or Trp53/Cdkn2a DKO gastric organoid colonies formed under ultra-low attachment culture conditions in WRN media after 21 days.

(c) Quantification and representative dissection microscope images of dys-Lgr5-p53^{KO} control or Cdkn2a DKO gastric organoid colonies formed under low-attachment culture conditions in indicated media after 7 days. Data presented as mean ± s.d. of three culture replicates; p-values calculated by two-sided Student's t-test.

(d) Primary xenograft growth of dys-Lgr5-p53^{WT} gastric organoids expressing either a control sgRNA, *Trp53* sgRNA, *Cdkn2a* sgRNA, or *Trp53*/*Cdkn2a* sgRNA (DKO) in nude mice (n=6 per group).

(**e)** Immunoblot showing protein levels of phospho-CHK1, total-CHK1, phospho-RPA32, p53, p16, and vinculin (loading control) in dys-Lgr5-p53^{WT} expressing either a control sgRNA, *Trp53* sgRNA, *Cdkn2a* sgRNA, or *Trp53*/*Cdkn2a* sgRNA (DKO). This experiment was repeated once.

(f) Heatmap showing relative sensitivity of CHEK1/2 inhibitor AZD7762 in 30 human gastric cancer cell lines. Solid red rectangles indicate cell-lines with co-disruption of *TP53*/*CDKN2A*; p-value = 0.0051, FDR = 0 (Top panel); Box plot showing quantiles of sensitivity

to CHEK1/2 inhibitor AZD77622 in 30 human gastric cancer cell lines (black dots) stratified into four molecular groups: CDKN2A^{WT}/TP53^{WT} (n = 8), CDKN2A^{altered}/TP53^{WT} (n = 1), CDKN2A^{WT}/TP53^{altered} (n = 15), and CDKN2A^{altered}/TP53^{altered} (n = 6). Drug response was measured as Area Under the Curve (AUC). Differences in sensitivity were determined by two-sided Student's t-test with *p-value <0.05 and **p-value < 0.01 (Bottom Panel)
(g) Dose-response curve of isogenic CP-A cell lines expressing either control sgRNA, p53 sg#1, or p53 sg#2 to indicated concentrations of Prexasertib. IC_{50} scores are displayed; Data presented as mean ± s.d. of six culture replicates at each indicated dose; Comparison of Fits, p value = 0.011 based on differences in IC_{50} (right panel). Immunoblot phospho-CHK1, phospho-ATR, total-ATR, and B-actin loading control in CP-A control or p53^{KO} BE cells treated with indicated concentrations of Prexasertib (left panel). This experiment was repeated once. **(h)** Dose-response curve of isogenic dys-Lgr5-p53^{WT}-control and dys-Lgr5-p53^{WT}-DKO gastric organoids to indicated concentrations of Prexasertib (Top). Comparison of Fits, p = 0.0001 based on bottom value. Dose-response curve of isogenic dys-Lgr5-p53^{KO}-control and dys-Lgr5-p53^{KO}-sg*CDKN2A* gastric organoids to indicated concentrations of Prexasertib. Comparison of Fits, p = 0.0047 based on IC_{50}. Data presented as mean ± s.d. of six culture replicates at each indicated dose
(i) Representative phase contrast images of dys-Lgr5-p53^{WT}-control, dys-Lgr5-p53^{WT}-DKO, dys-Lgr5-p53^{KO}-control, dys-Lgr5-p53^{WT}-p16^{KO} gastric organoids treated for 36 hours with DMSO or indicated concentration of CHK1/2 inhibitor Prexasertib. This experiment was repeated once.
(j) Quantification of organoid size from each group in experiment (F). Data presented as mean ± s.d. of seven technical replicates; p-values calculated by two-sided Student's t-test.
(k) Schematic of functional and therapeutic role of *CDKN2A* and *TP53* alterations in gastric premalignancy